The PARIS Ocean Altimeter In-Orbit Demonstrator

Manuel Martín-Neira, *Senior Member, IEEE*, Salvatore D'Addio, *Member, IEEE*, Christopher Buck, Nicolas Floury, *Member, IEEE*, and Roberto Prieto-Cerdeira, *Member, IEEE*

***Abstract*—Mesoscale ocean altimetry remains a challenge in satellite remote sensing. Conventional nadir-looking radar altimeters can make observations only along the satellite ground track, and many of them are needed to sample the sea surface at the required spatial and temporal resolutions. The Passive Reflectometry and Interferometry System (PARIS) using Global Navigation Satellite Systems (GNSS) reflected signals was proposed as a means to perform ocean altimetry along several tracks simultaneously spread over a wide swath. The bandwidth limitation of the GNSS signals and the large ionospheric delay at L-band are however issues which deserve careful attention in the design and performance of a PARIS ocean altimeter. This paper describes such an instrument specially conceived to fully exploit the GNSS signals for best altimetric performance and to provide multifrequency observations to correct for the ionospheric delay. Furthermore, an in-orbit demonstration mission that would prove the expected altimetric accuracy suited for mesoscale ocean science is proposed.**

***Index Terms*—Global Navigation Satellite Systems (GNSS) reflectometry, ocean altimetry, passive reflectometry and interferometry system (PARIS) concept.**

I. Introduction

MESOSCALE ocean altimetry remains being a challenging area for satellite observations and yet of great interest for oceanographers trying to validate and drive their ocean circulation models with real measurements. Since the very first spaceborne altimeters onboard Skylab, GEOS-3, and SeaSat back in the 1970s [1], little has changed in the fundamental way of performing ocean altimetry from space, i.e., by using a nadir-looking radar.

Ad hoc constellations of a few of such nadir-looking altimeters [2] are being exploited to increase the spatial and temporal sampling of the ocean. There have even been proposals to embark many radar altimeters on large constellations of commercial communication satellites, such as onboard the satellites of the next generation of Iridium's space segment.

In parallel, several concepts have been put forward to extend altimetry to the side of the satellite track, including the following: 1) bistatic radar within a constellation of cooperative radar altimeters [3]; 2) radar interferometry from a single satellite [4]–[6]; and 3) bistatic radar using Global Navigation Satellite Systems (GNSS) reflected signals [7] (Fig. 1). This paper deals with the latter concept which will be referred to as Passive Reflectometry and Interferometry System (PARIS).

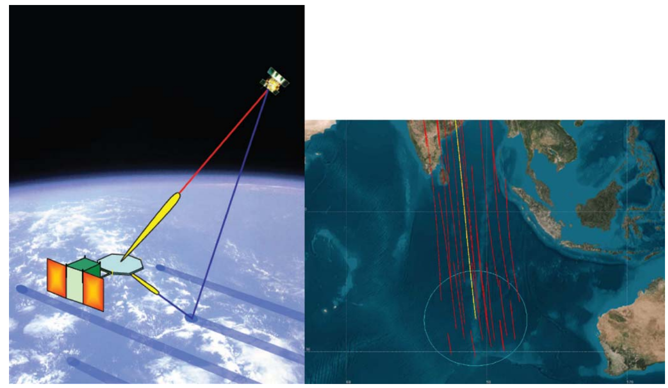

Fig. 1. (Left) PARIS-IoD concept. (Right) Typical sampling characteristics.

The PARIS altimeter is a new type of passive instrument which combines bistatic radar and radiometer techniques, including interferometry. As will be described throughout this paper, this combination enables optimal use of the spectrum of the GNSS signals for precise ranging, accurate correction of the ionospheric delay, and fine amplitude and delay calibration. The main advantage of PARIS is its synoptic sampling capability, which, assuming the deployment of five GNSS constellations in the future, could be over 20-fold that of a single nadir-looking altimeter (Fig. 1). Ultimately, this instrument is conceived to match a mesoscale ocean requirement of 5-cm height accuracy, 100-km along-track spatial resolution (10 km across track), two-day revisit time, and global coverage. This is equivalent to 7 cm in 50 km $\times$ 10 km. The configuration of an In-orbit Demonstrator (IoD) carrying a reduced-size PARIS altimeter on a small satellite platform is presented.

II. Objectives and System Concept

A. Why PARIS IoD

The PARIS IoD has been conceived to take the next step toward proving the case for GNSS-based mesoscale ocean altimetry. More fundamentally, the PARIS IoD aims at demonstrating the scientific applications of the GNSS. In the last 15 years, many challenges have been faced, and resolutions or workarounds were found such as the impact of speckle in the models, using multiple frequencies to correct for the effects of the ionosphere, and, most recently, use of the autocorrelation function (ACF) to allow the full bandwidth of the available signals to be used without knowledge of the actual codes.

PARIS IoD will pick up where UK-DMC left off [8], [9]. The Surrey Satellite Technology Ltd. GPS reflectometry instrument onboard UK-DMC was groundbreaking in that it was

Manuscript received July 17, 2009; revised August 30, 2010; accepted October 31, 2010. Date of publication January 5, 2011; date of current version May 20, 2011.

The authors are with the European Space Research and Technology Centre (ESTEC), European Space Agency, 2200 AG Noordwijk, The Netherlands (e-mail: manuel.martin-neira@esa.int).

Color versions of one or more of the figures in this paper are available online at http://ieeexplore.ieee.org.

Digital Object Identifier 10.1109/TGRS.2010.2092431

the first spaceborne instrument dedicated to the reception of Earth-reflected signals and, successful as it was, it was never intended nor designed to demonstrate ocean altimetry. Among other issues, it received only L1, and hence, ionospheric errors could not be corrected. Moreover, the antenna gain was too low (< 12 dBic) to provide sufficient signal-to-noise ratio (SNR). That aside, UK-DMC showed conclusively that reflected GPS signals could be reliably retrieved over oceans of varying degrees of roughness and that the information contained in the signal could be used for scatterometric purposes. Reflected signals were also captured over land, and those picked up over sea ice pointed the way to yet another potentially valuable application of GNSS-R, namely, sea-ice freeboard estimation.

PARIS IoD is aimed specifically at altimetry, and the instrument has been designed accordingly. Nevertheless, this does not preclude other applications such as the ones explained next being explored with this instrument.

B. Secondary Objectives

1) Scatterometry: GNSS signals reflected off the surface of the ocean contain, completely analogously with conventional radar altimeters, information related to the surface roughness due to the action of wind and currents. Zavorotny and Voronovich [10] were the first to derive a model to predict the shape of the correlated reflected signal under the influence of surface roughness conditions as dictated by the Elfouhaily spectrum [11]. This model has since been successfully used to invert results obtained with a variety of GNSS-R sensors, including that of the UK-DMC satellite. The same basic technique has also been used in a nearly routine way to determine the directional mean-squared slope of the sea surface during preparatory airborne campaigns for the forthcoming SMOS mission whereby the sea surface must be known in order to correct the ocean salinity signal recorded by the radiometer.

PARIS IoD, with its multiple agile beams (see below), will be able to progress understanding of GNSS-R scatterometry owing to increased SNR and accurate calibration.

2) Ice Altimetry: One of the most tantalizing results coming from the UK-DMC mission was the signals retrieved over sea ice. What was apparently demonstrated by Gleason [9] was that not only that the reflected signals could be reliably collected off sea ice but also the signal strengths were often surprisingly strong and that this allowed the phase of the signal to be determined to a reasonable level of confidence. These phases were observed to increase or decrease nearly linearly over time which was very suggestive of phase wrapping due, in the main, to the changing geometry between transmitter and receiver. Indeed, it was possible, at least over short periods of time, to unwrap the phase, and this gives rise to the possibility of phase altimetry which is, of course, much more precise than code altimetry. The PARIS-IoD instrument, with its better SNR, improved orbital knowledge, and multiple-frequency capability will be able to provide much more and better data over sea ice with which it will be possible to demonstrate ice altimetry and, hence, ice freeboard demonstration. This is of major interest for climate change research and one of the main objectives of the CryoSat mission.

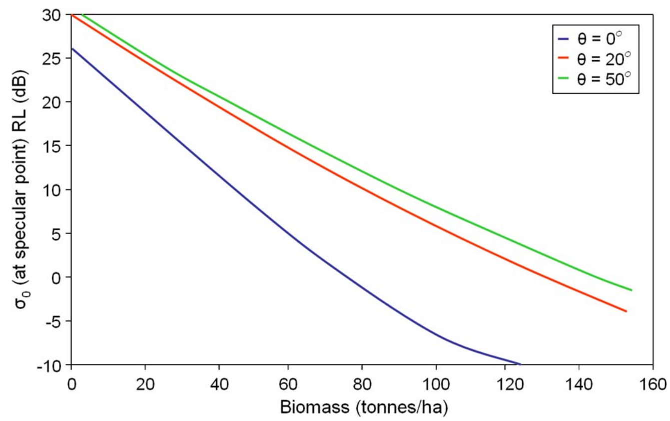

Fig. 2. Impact of biomass on forward scatter of L-band signals at various incidence angles.

3) Soil Moisture: All current GNSS systems operate in L-band which is the same part of the spectrum selected for the SMOS mission due to the sensitivity of this frequency band to soil moisture. Airborne campaigns, e.g., SMEX02, have already demonstrated the impact of soil moisture on land-reflected GPS signals, and recent work carried out in an ESA contract has attempted to derive soil-moisture content from these signals. Again, UK-DMC has shown that it is possible to collect reflected signals from land surfaces in space and that PARIS IoD will be able to provide a valuable alternative source of soil-moisture signals which could complement those obtained by SMOS (or a follow-on mission thereof) [45].

4) Biomass: A recent ESA study into the use of bistatic microwave measurements for Earth observation looked, among other things, at potential applications for forward scattered signals of opportunity, e.g., GNSS signals [45].

What emerged was that, for a right-hand circularly polarized incident signal, the signal power received by a left-hand circularly polarized antenna would, for low incidence angles, decrease nearly linearly in logarithmic scale (in decibels) with increasing biomass (see Fig. 2) with no indication of saturation until well over 150 t/ha. Although this is likely to be insufficient for tropical rainforest biomasses, it does open the possibility for mapping boreal biomass. A well-calibrated PARIS-IoD instrument would be perfectly suited to provide high-quality data for testing this hypothesis.

C. System Constraints

The PARIS IoD aims at demonstrating the scientific applications of GNSS, particularly mesoscale ocean altimetry. The PARIS IoD is currently framed within the Element-4 of ESA's latest General Support and Technology Program (GSTP-5) which covers in-orbit demonstration of key technologies and techniques. PARIS altimetry has reached the stage where further theory and airborne research will not be able to demonstrate the full potential of the technique, and hence, it is the right time for a representative spaceborne demonstrator.

GSTP-5 Element-4 has a given budget envelope for low-cost IoDs that should include all aspects of the mission: payload, platform, launch, and operation. Moreover, the platform is

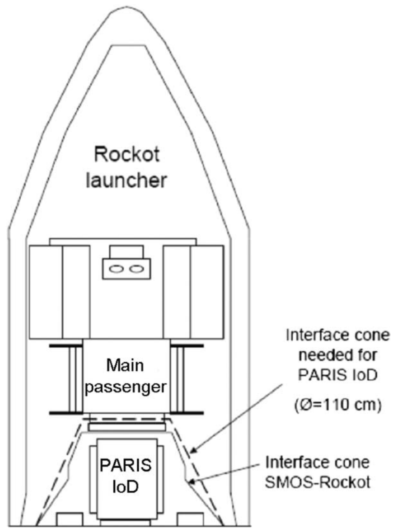

Fig. 3. Rockot fairing showing position of PARIS IoD in the cone beneath a main passenger in a double-launch configuration similar to that of SMOS and Proba-2.

prescribed as minisatellite class. This limits the scope of any mission to relatively modest proportions in terms of payload mass, which for this class of satellite should be less than 50 kg, and payload average power consumption, which should be in the 40–60-W range.

For the PARIS altimeter, the altimetric performance is dependent, in the first place, on the overall SNR which is basically dictated by the size of the antenna but which also requires a good design of the beamforming network and low-noise amplifiers. The beamformer is required because multiple antenna beams are desired which must be steerable to the specular points, as will be later described.

In order to correct for the effects of the ionosphere, a minimum of two GNSS frequencies is required. Nominally, these will be the GPS L1—GALILEO E1 (1575.42 MHz) and GPS L5—GALILEO E5a (1176.45 MHz) bands since these provide the greatest separation in frequency and, hence, the best accuracy for the ionospheric delay incurred.

A further constraint is the very high raw data rate which, for four up- and downlooking beams, is in the range of some gigabits per second. With onboard processing and depending on the integration time used, this can be reduced to a few megabits per second. This makes the downlinking of the data tractable with a relatively modest downlink transponder but places an additional burden on the mass and power budgets for the onboard processor and associated memory.

Clearly, the choice of launcher is a critical issue in terms of cost and availability. Some likely candidates are Rockot or Soyuz. Ultimately, the choice will depend on a suitable "host" mission since a dedicated launch would be too expensive, meaning that PARIS IoD will have to be launched as a secondary "piggyback" satellite.

Taking as an example the launch of SMOS and Proba-2 on Rockot (Fig. 3), where PARIS IoD would be installed as a secondary satellite inside the interface cone between the main satellite passenger and the launcher, there is an obvious constraint on the maximum size of nonfolded antenna that can be accommodated which, in this case, is approximately 110 cm. This is commensurate with the minimum diameter antenna determined to be viable for demonstrating mesoscale ocean altimetry.

D. System Concept

Although based soundly on previous ground-based airborne and spaceborne concepts of a GNSS reflectometer, the PARIS-IoD concept includes a subtle major progression. In common with the existing PARIS Airborne Demonstrator (PAD), it makes use of a phased array antenna with four high gain beams to collect the reflected signals, but in place of a modest-gain wide-beam antenna for the direct signals, PARIS IoD has instead an identical phased array antenna producing four high gain beams as for the downlooking antenna. The only difference is the polarization, with the direct antenna being right-hand circularly polarized rather than left-hand circularly polarized as for the downlooking antenna. This difference is to cope with the fact that the polarization changes from right hand to left hand after reflection from the sea surface.

The reason for the high-gain direct antenna requirement is that, unlike other reflectometers which use replicas of the GNSS codes to correlate with the direct and reflected signals, PARIS IoD makes use of the composite ACF of all the codes in the entire allocated band. The observables are therefore obtained by directly cross-correlating the direct and reflected signals. The effect, however, is that the processing gain (some 20 dB) is lost, and hence, a higher antenna gain is required to compensate this loss. What this brings though is the possibility to use the full GNSS bandwidth of roughly 20–50 MHz per band regardless of whether the codes are known or not. For example, GALILEO E1 (or GPS L1 and L5) and GALILEO E5 bandwidths are 25 and 50 MHz wide, respectively [12].

As already mentioned, PARIS IoD will use dual-frequency observations to allow precise estimation of the ionospheric delay and will incorporate precise onboard delay and amplitude calibration. To achieve this, two antenna arrays (up and downlooking) are mounted back-to-back–minimizing their physical separation–with corresponding elements being paired through a mutual calibration switch circuit, allowing them and the analog beamforming networks to be fully characterized. In addition, it is intended periodically to rotate the otherwise nadir-pointed satellite through 180° in order to allow the normally downfacing antenna to take noise measurements of the cold sky. This will result in highly accurate amplitude calibration being possible which is beneficial to the achievable overall altimetric accuracy as well as to the enabling of the secondary applications.

The equipment to be built for PARIS IoD includes the following:

1) up- and downlooking antennas;
2) radio-frequency front ends;
3) analogue beamforming networks;
4) harness between front ends and beamformers;
5) downconverter and analog-to-digital converter;
6) correlator unit;
7) instrument controller;

TABLE I
PARIS INSTRUMENT MASS BUDGET

No of array elements	31+31
Radiators + structure	20kg
62 LNAs	3kg
Harness	6kg
Mechanisms	3kg
BFN (phase shifters)	2kg
Processor + power conditioning	6kg
X-band transmitter and antenna	3kg
Total	**44kg**

TABLE II
PARIS INSTRUMENT POWER BUDGET

Item	**Power**
LNAs (62x0.4W)	25W
Signal Processor	12W
Solid-State Mass Memory	5W
Instrument Control Unit (ASIC)	4W
Downlink Average	1W*
Total	**47W**

* Downlink DC power of 15W with 7% duty cycle

8) downlink system;
9) deployment mechanism.

As already explained, the antennas will be around 110 cm in diameter and consist nominally of 31 elements arranged in an 1-6-12-12 hexagonal grid. For the beamforming network, suitable monolithic microwave integrated circuits will be used, including some developed in previous ESA contracts. The correlator unit can be largely based on the field-programmable-gate-array-based signal processor developed for PAD, but using a suitable radiation-tolerant device, or on application-specified integrated-circuit technology.

The downlink, assuming use is made, for instance, of a 13-m antenna on Svalbard and allowing for a data rate of about 10 Mb/s, will require a downlink transmit power of some 2.5 W.

From the initial investigations carried out at the European Space Research and Technology Centre (ESTEC), first estimates of the main budgets have been derived covering the payload mass (Table I) and power consumption (Table II).

III. INSTRUMENT PERFORMANCE

A. Choice of the Instrument Baseline

As already introduced earlier, the adoption of direct cross-correlation between the direct and reflected navigation signals (i.e., interferometric processing) allows maximizing the height precision of the instrument since the full power spectral density is exploited for range estimation. However, with respect to the conventional PARIS configuration, which performs the cross-correlation with onboard generated replica of open-access codes, the interferometric configuration would experience a degradation of SNR at the cross-correlator output and, consequently, a degradation of height precision. The performance degradation due to the presence of thermal noise in both inputs of the cross-correlation is analyzed in the following paragraphs, and it will be shown that it can be arbitrarily reduced by appropriate sizing of the uplooking antenna.

However, there is another reason that makes the interferometric processing unique. Indeed, the selection of the PARIS altimeter architecture, which exploits the interferometric processing, is essential since it is, at present, the only configuration that makes the PARIS altimeter fulfill the mesoscale altimetry accuracy requirement. Generally speaking, the PARIS height estimation is affected by random zero average height error (commonly referred to as the height precision) and by additional random and deterministic errors that affect the total absolute measurement error or accuracy. Typical causes of additional error are propagation effects such as the ionospheric and tropospheric delay and electromagnetic scattering effects, such as electromagnetic bias and skewness bias. In particular, the ionospheric delay is the major cause of absolute ranging error at L-band as it can reach tens of meters. The ionospheric delay, being a frequency dispersive effect, is typically corrected in conventional altimetry as well as in GNSS precise positioning by combining measurements performed at two widely separated frequencies. As an example, a conventional PARIS altimeter exploiting open-access GPS navigation signals would not be able to correct the ionospheric delay down to centimeter level accuracy. This is simply due to the narrow bandwidth of open-access navigation signals at GPS L1 and L2 which limits the achievable range precision at these bands to a few decimeters, far above the centimeter precision requested for mesoscale altimetry. Thus, this noisy measurement would severely affect the absolute accuracy when combined with the high-precision measurement of the wider band L5 signal, as typically performed to estimate the ionospheric delay. On the other hand, the adoption of the interferometric processing implies the availability of high-precision measurements for all the transmitted frequencies and for all the GNSS systems; thus, the ionospheric delay can be corrected as explained later. This characteristic distinguishes the interferometric processing from the conventional GNSS altimetry adopting open-access codes.

B. Instrument Architecture

The PARIS altimeter basically consists of a double phased array that is able to steer high-gain beams toward the GNSS transmitters as well as in parallel toward their corresponding specular points, as shown in Fig. 4. The received direct signal is first amplified, bandpass filtered, and in-phase and quadrature downconverted using a local oscillator (LO) frequency at the nominal center frequency of a particular GNSS band (for example, GALILEO E1). The intermediate-frequency (IF) direct signal is then shifted in frequency to match the Doppler shift of the reflected one owing to a precise numerically controlled oscillator (NCO). The frequency shift f_s can be determined from the knowledge of the GNSS and PARIS satellite positions and velocities and the position of the specular reflection point on the Earth surface, all derived by the onboard computer. The onboard computer receives accurate orbit information of the GNSS satellites from the ground through an uplink and, in addition, the time, position, and velocity of the PARIS-IoD satellite itself from the onboard navigation receiver. The estimation of the Doppler shift f_s, performed in real time, is

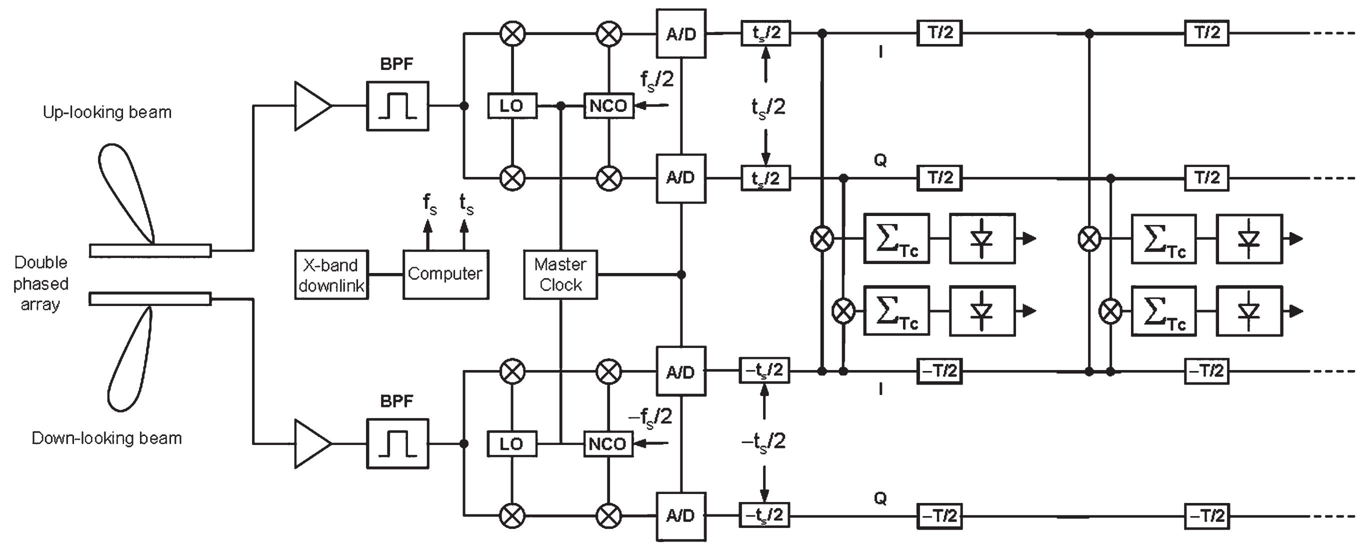

Fig. 4. PARIS altimeter high-level architecture (QQ and IQ products not shown).

used to continuously steer the NCO. The frequency-shifted direct signal is digitized and time shifted to compensate for the additional delay of the reflected signal path. The amount of time shift T_s is computed from the known geometry, similarly to the Doppler estimation. The frequency- and time-shifted direct signal is then complex cross-correlated with the received reflected signal. The cross-correlation is evaluated at a time lag resolution T and with a number of lags compatible with the code chip rates and length of the waveform to be observed. The cross-correlation is performed over a time that guarantees the coherence of the ocean scattered signal. The cross-correlation waveforms are further accumulated incoherently to reduce speckle, thermal noise, and data rate onboard. These averaged waveforms are stored onboard until they are downlinked to ground. Further incoherent averaging may be performed by the ground processor.

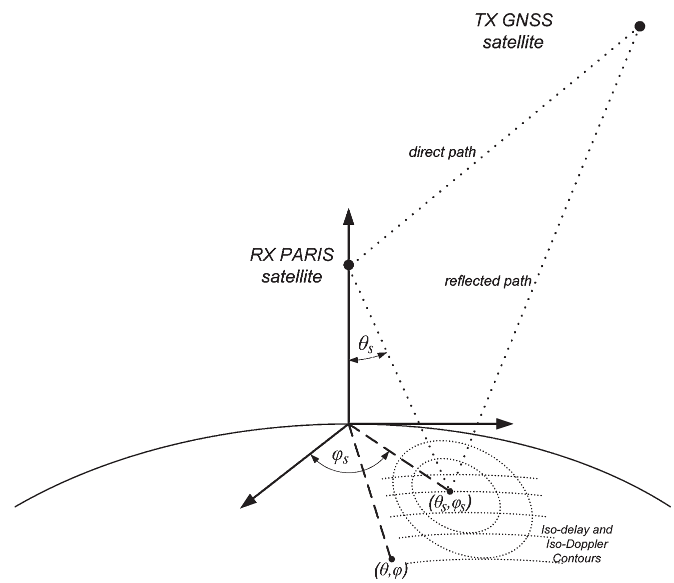

Fig. 5. Bistatic geometry involved in the PARIS concept.

C. Correlation Characteristics of Composite GNSS Signals

The main advantage of the proposed PARIS interferometric processing is that it allows exploiting the full power spectral density of the transmitted GNSS signals in space. Hence, as will be shown in the following sections, the height estimation precision is always maximized. In addition, the interferometric processing can be performed by adopting a simple, flexible, and robust instrument architecture.

In this section, as an example, the correlation properties of the GPS L1 composite signal are analyzed. The corresponding PARIS altimetry power waveforms are then derived and compared with the one that would have been obtained by adopting the conventional processing which exploits only known navigation open-access codes, such as the C/A code. In particular, the ACF and the reflected power waveform characteristics of the GPS L1 signal are compared.

As derived in Appendix I, for a given center frequency f_c, the average power altimetry waveform $\langle|Z_S(t,\tau)|^2\rangle$ can be analytically represented in its simplest form as the 2-D convolution of the ocean scattered power $P_R(\theta,\varphi)$ and the magnitude-squared Woodward ambiguity function U of the composite GNSS signal [9], [14], [21]

$$\left\langle |Z_S(t,\tau)|^2 \right\rangle = P_R\left(\theta,\varphi\right) \underset{\theta,\varphi}{\otimes} \left|U\left(\Delta\tau\left(\tau(\theta,\varphi)\right), \Delta f(\theta,\varphi)\right)\right|^2 \tag{1}$$

where t is the time instant at which the cross-correlation is performed and (θ,φ) represent the spatial coordinates over the sea surface (see Fig. 5). In (1), the contribution of significant wave height introduced later in (80) has been neglected.

Therefore, as is well known and expressed in (1), the properties of the altimetry power waveform are intrinsically related to the time–frequency discrimination properties of the composite GNSS signal and, in particular, of the corresponding ambiguity function.

As a reference case, the reflected cross-correlation power waveform characteristics for the different composite signals are analyzed for a particular reference mission scenario, as

TABLE III
SIMULATION SYSTEM PARAMETERS

Parameter	Value	Unit
Orbit Altitude	800	Km
Specular Point Incidence Angle	35	deg
Wind Speed at sea level	10	m/s
Up-looking and Down-looking Antenna Gain	23	dBi
Receiver Bandwidth	30	MHz
Coherent integration Time	1.5	ms
Along-Track Spatial Resolution	100	Km

TABLE IV
GPS L1 SIGNAL OVERVIEW

Signal	Modulation	EIRP
C/A code (civil)	BPSK-R(1)	28 dBW
P(Y) code (encrypted)	BPSK-R(10)	25 dBW
M code (encrypted)	BOC(10,5)	29.5 dBW

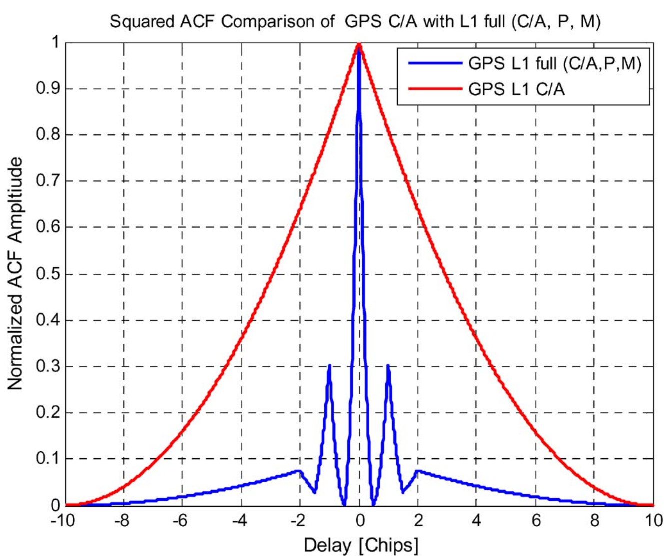

Fig. 6. Squared ACF of composite GPS L1 and C/A components.

presented in Table III. For simplicity, in this analysis, the effect of sea surface significant wave height has not been included. It is worth mentioning that the mission parameters are presented for a possible demonstration mission (the orbit altitude for an operational mission would be much higher, i.e., 1500 km, as will be shown later in the system design section).

The planned GPS L1 composite signal will be composed by three different signals distributed among the in-phase and in-quadrature channels: the C/A, P, and M components [22], [23]. The main characteristics of these signal components and the reference equivalent isotropically radiated power considered in this paper are given in Table IV.

In Fig. 6, the ideal magnitude-squared ACF characteristics of the composite GPS L1 signal are compared against those of its civil component GPS L1 C/A. The delay is expressed in chips, where a reference chip rate of 10 Mchips/s is considered. As expected, due to the wider bandwidth of the composite signal, the composite GPS L1 ACF is much narrower than the C/A code only, hence guaranteeing improved altimetry precision.

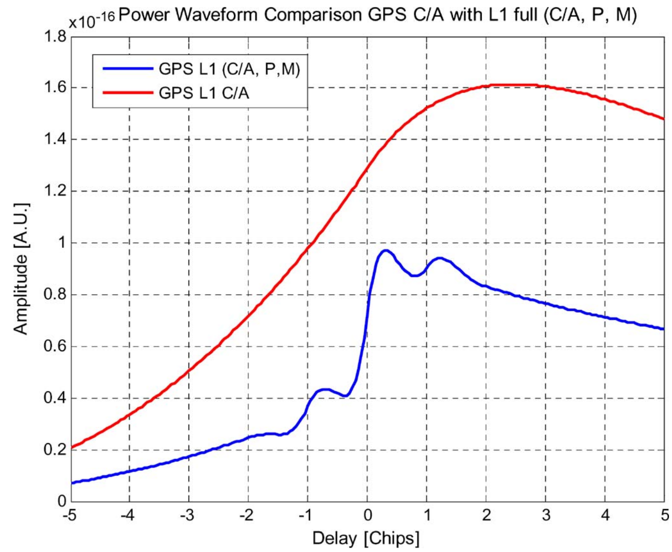

Fig. 7. Composite GPS L1 and C/A code reflected power waveforms.

The corresponding reflected power waveforms are compared in Fig. 7. The reference C/A power waveform shows higher power level at the zero delay point (i.e., the altimetry tracking point, corresponding to the delay of the bistatic specular point, as imposed by simulation) with respect to the composite GPS L1. This is simply due to the larger width of the C/A ACF, as shown earlier, which extends in a range from -10 to $+10$ chips. This property implies that, in the C/A code case, the power scattered off a wider sea area is contributing to the reflected cross-correlation waveform with respect to the full composite GPS L1. On the other hand, as expected, on the zero delay point, the GPS L1 composite waveform is much steeper than the C/A curve (due to the wider processed bandwidth of the GPS L1), leading to better altimetry precision, as will be shown later. The main conclusion is that the interferometric processing provides more precise ranging due to the steeper slope of the power waveform on the tracking point (the point of maximum slope in the rising edge) with an acceptable degradation in signal amplitude.

D. Interferometric Processing

In this section, the basic theory of the interferometric processing is presented, and the average signal-to-thermal noise ratio at the output of the cross-correlator is analytically derived.

As introduced previously, the interferometric processing consists of performing the complex cross-correlation between the received direct and reflected signals. This allows accurate estimation of their relative delay without the need to generate any replica of the modulating codes onboard. Moreover, all embedded codes in a given GNSS frequency band do contribute to the cross-correlation shape, including the high-chip-rate restricted access codes, thus obtaining the best ranging performance for altimetry. In other words, the interferometric processing allows exploiting the full power spectral density of the GNSS signals, thus improving the ranging precision. However, in order to evaluate the ranging performance of the altimeter, it is fundamental to analyze the SNR at the output

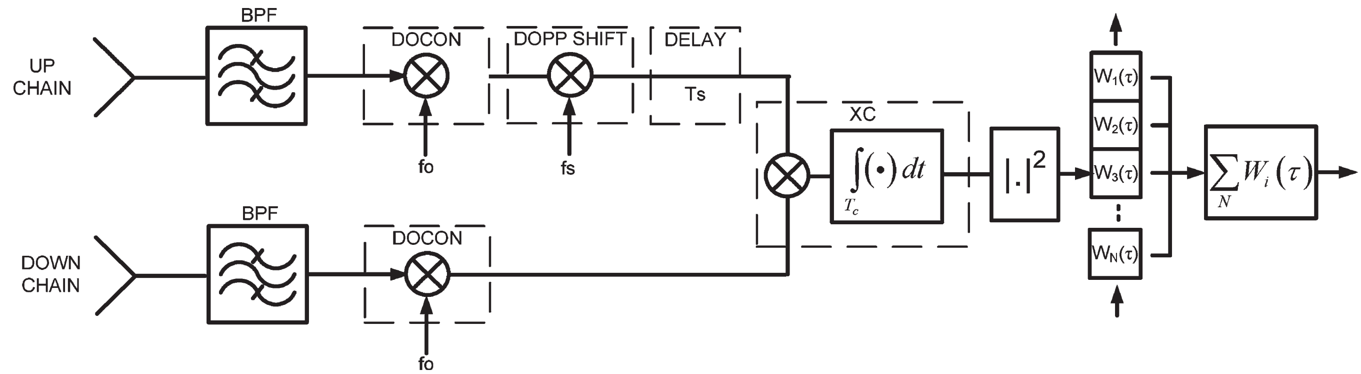

Fig. 8. Schematic diagram of the PARIS altimeter processing.

of the cross-correlation. The SNR is a critical parameter for the interferometric processing configuration, since it is affected by thermal noise at both uplooking and downlooking chains. This, in turn, has a major impact on the sizing of both up- and downlooking antennas.

The reference instrument scheme is shown in Fig. 8. The received direct signal v_d is bandpass filtered, downconverted, Doppler-shifted, and time delayed, as well as the received reflected signal v_r. The two signals are then cross-correlated for a time period T_c. Then, the amplitude squared (i.e., power) of the correlator output $Z(\tau)$ is obtained and further accumulated over N_{inc} samples. By representing both the received direct and reflected signals as the sum of the useful signal $s(t)$ and thermal noise $n(t)$ components, the cross-correlation output can be represented as

$$\begin{aligned} Z(t,\tau) =& \frac{1}{T_c}\int_{\frac{-T_c}{2}}^{\frac{+T_c}{2}} v_r(t+t') \quad v_d^*(t+t'-\tau)\,dt' \\ =& \frac{1}{T_c}\int_{\frac{-T_c}{2}}^{\frac{+T_c}{2}} s_r(t+t')s_d^*(t+t'-\tau)\,dt' \\ &+\frac{1}{T_c}\int_{\frac{-T_c}{2}}^{\frac{+T_c}{2}} s_r(t+t')n_d^*(t+t'-\tau)\,dt' \\ &+\frac{1}{T_c}\int_{\frac{-T_c}{2}}^{\frac{+T_c}{2}} n_r(t+t')s_d^*(t+t'-\tau)\,dt' \\ &+\frac{1}{T_c}\int_{\frac{-T_c}{2}}^{\frac{+T_c}{2}} n_r(t+t')n_d^*(t+t'-\tau)\,dt' \\ =& Z_S(t,\tau)+Z_{Nd}(t,\tau)+Z_{Nr}(t,\tau)+Z_{Ndr}(t,\tau). \end{aligned} \tag{2}$$

Therefore, by considering that the signal and the up- and downlooking thermal noise components are uncorrelated to each other, the average power at the correlator output is given by the sum of four power terms

$$\begin{aligned} \left\langle |Z(\tau)|^2 \right\rangle = \left\langle |Z_S(\tau)|^2 \right\rangle + \left\langle |Z_{Nd}(\tau)|^2 \right\rangle \\ + \left\langle |Z_{Nr}(\tau)|^2 \right\rangle + \left\langle |Z_{Ndr}(\tau)|^2 \right\rangle. \end{aligned} \tag{3}$$

An analytical expression for each of the four cross-correlation power terms is derived in detail in Appendix I. It results in the fact that the average SNR at the output of the correlator can be simply related to the SNR that would be obtained in the ideal case where no thermal noise was present in the received direct signal (hereinafter referred to as the clean replica case, SNR_{cr}) and to the SNRs of the direct and reflected channels (SNR_D and SNR_R, respectively) at the input of the cross-correlator

$$\begin{aligned} SNR(\tau) &= \frac{\left\langle |Z_S(\tau)|^2 \right\rangle}{\left\langle |Z_{Nd}(\tau)|^2 \right\rangle + \left\langle |Z_{Nr}(\tau)|^2 \right\rangle + \left\langle |Z_{Ndr}(\tau)|^2 \right\rangle} \\ &= \frac{SNR_{cr}}{\left[1+\frac{1+SNR_R}{SNR_D}\right]}. \end{aligned} \tag{4}$$

Equation (4) is very powerful since it allows comparing the SNR of the interferometric processing to the SNR_{cr} achievable if all the navigation codes were known and, hence, if it were possible to perform a cross-correlation with a clean replica of the navigation signal generated onboard. It is evident that the fraction in the denominator of (4) represents the loss in SNR due to the adoption of the interferometric processing. A graceful SNR degradation is obtained if the following relation holds:

$$SNR_D \gg 1 + SNR_R. \tag{5}$$

It is apparent that (5) can be satisfied by appropriate sizing of the up- and downlooking antennas. The correct sizing makes the SNR of the interferometric processing comparable to that obtained when using clean codes, at the expense of increased mass and complexity for the uplooking antenna. However, the fact that some codes cannot be replicated onboard because of their restricted access gives a clear advantage to the straight direct cross-correlation exploited in the interferometric processing over the use of clean codes.

As a reference, in the following, the power reflected cross-correlation SNR corresponding to the composite GPS L1 signal is analyzed. As presented in (92) in Appendix I, the SNR for the clean replica case is generally given by

$$\begin{aligned} &SNR_{cr}(t,\tau) \\ &\quad = \frac{T_c\left[P_R(\theta,\varphi)\otimes_{\theta,\varphi}\left|U\left(\Delta\tau\left(\tau(\theta,\varphi)\right),\Delta f(\theta,\varphi)\right)\right|^2\right]}{kT_{Nr}} \end{aligned} \tag{6}$$

where T_c is the cross-correlation integration time, k is the Boltzmann constant, and T_{Nr} is the equivalent noise temperature of the downlooking chain.

By simply adopting (6) and considering the reference scenario introduced in Table III, the reflected power waveform SNR for the composite GPS L1 yields $SNR_{cr} = 6.3$ dB in the case of adoption of clean replica codes. The corresponding downlooking SNR at the cross-correlator input is equal to $SNR_R = -22$ dB. Then, in order to obtain a negligible SNR degradation, (5) should be satisfied, yielding to $SNR_D \gg 0$ dB. If, for simplicity, a gain value of 23 dBi is considered for the uplooking antenna (same as for the downlooking one), the corresponding SNR at the cross-correlator input would be $SNR_D = 2.9$ dB. This yields a global SNR degradation of 1.8 dB, equivalent to a total reflected power waveform SNR for the interferometric case of 4.5 dB. If lower total SNR degradation is required, the SNR_D in the uplooking chain should be increased. This can only be achieved by increasing accordingly the uplooking antenna gain and, hence, its physical dimensions.

However, as will be shown later, an SNR degradation such as 1.8 dB will not result in any major degradation in terms of height precision. This is because the precision is dominated by speckle, once sufficient SNR (i.e., $> 5-6$ dB) is achieved by proper uplooking antenna sizing and optimum selection of the coherent integration time T_c.

E. Altimetric Tracking Point

In order to measure the sea surface height, the range corresponding to the specular reflection point shall be measured accurately. For this reason, the knowledge of the exact position of the specular point on the power reflected waveform appears to be of fundamental importance for optimizing the instrument architecture and postprocessing strategy and, thus, the final altimetry performance.

As is well known in conventional nadir-looking altimetry, the range measurement is performed with respect to the minimum range point, which corresponds to the position of the peak of the derivative of the waveform leading edge, and corresponds as well to the half-power point with respect to the peak of the waveform [24]. This is not always the case for a PARIS altimeter: The specular point does correspond to the position of the maximum derivative on the leading edge [38]. This is due to the large coherent integration time adopted in the coherent processing which causes a spatial filtering of the power scattered off the ocean surface; the waveform power at the specular delay exceeds the half-power point [21]. It is shown in [38] that, depending on the frequency response of the GNSS-R receiver and/or the sea state conditions, the derivative peak position may have a bias with respect to the one of the specular point. However, this bias can be modeled, predicted, and taken properly into account in the waveform-retracking process.

F. Altimetric Precision

In this section, the achievable precision of the PARIS altimeter is analyzed by means of an approximated analytical model. Generally speaking, the prediction of the height estimation precision is of fundamental importance for proper design and sizing of the overall instrument. In the last years, a few models have been proposed, addressing the analysis from very different approaches. The first code range precision model was proposed by Lowe [19]. This model simply extends the code range precision of direct navigation signals to those reflected by the sea surface. The main limitation of this model is that it is strictly valid for high values of signal-to-thermal-noise ratio and it neglects the impact of fading noise in range precision estimation. A more comprehensive model has been proposed later by Germain [20], based on the Cramer–Rao Bound (CRB) approach. The CRB method allows predicting the best achievable performance in estimation problems for which the stochastic nature of the observation can be described by a probability density function.

A simpler and yet effective model is adopted in this paper, which has the main objective of intuitively analyzing the sensitivity of the height precision with respect to the different parameters such as the SNR, the observation geometry, the speckle, and the autocorrelation properties of composite GNSS transmitted signals. Similar approaches have been adopted to predict the height precision of conventional radar altimeters and radar scatterometers [18], [26].

As introduced in (3), the average cross-correlation power is the sum of the average cross-correlated useful power ($\langle |Z_S(\tau)|^2\rangle$) and of the average cross-correlated noise power terms ($\langle |Z_{Nd}(\tau)|^2\rangle + \langle |Z_{Nr}(\tau)|^2\rangle + \langle |Z_{Ndr}(\tau)|^2\rangle$). Rewritten as a sum of a signal and a noise term

$$\begin{aligned}\overline{P}_{Z,R} &= \left\langle |Z(\tau)|^2 \right\rangle \\ &= \left\langle |Z_S(\tau)|^2 \right\rangle + \left\langle |Z_{Nd}(\tau)|^2 \right\rangle \\ &\quad + \left\langle |Z_{Nr}(\tau)|^2 \right\rangle + \left\langle |Z_{Ndr}(\tau)|^2 \right\rangle \\ &= \overline{P}_{Z,S} + \overline{P}_{Z,N}. \end{aligned} \tag{7}$$

The power of the cross-correlation waveform can be further represented as a function of the signal power waveform and the SNR

$$\begin{aligned}\overline{P_{Z,R}} &= \overline{P_{Z,S}} + \overline{P_{Z,N}} \\ &= \overline{P_{Z,S}}\left(1 + \frac{\overline{P_{Z,N}}}{\overline{P_{Z,S}}}\right) \\ &= \overline{P_{Z,S}}\left(1 + \frac{1}{SNR}\right). \end{aligned} \tag{8}$$

The thermal noise component closely obeys circular complex Gaussian statistics. By invoking the central limit theorem, with the reflected field being the random phasor sum of the fields from many scatterers, the ocean scattered field may also be approximated with Gaussian statistics, for the purpose of our derivations. Under this assumption, the amplitude of the complex cross-correlation obeys Rayleigh statistics, and hence, the power of the cross-correlation is expected to have a negative exponential distribution, which features a mean equal to the standard deviation [36]. This effect is well known in literature as fading speckle or self-noise, since it is a multiplicative noise term independent from the instrument receiver front-end characteristics.

In order to reduce the standard deviation of the reflected power waveform due to speckle, incoherent averaging has to be performed over successive power waveforms. If N_{inc} independent successive power waveform samples at a generic delay lag are averaged, the amplitude standard deviation σ_R of the total received waveform power $P_{Z,R}$ is simply given by

$$\sigma_R = \frac{\overline{P_{Z,S}}}{\sqrt{N_{\mathrm{inc}}}}\left(1+\frac{1}{SNR}\right) \tag{9}$$

and similarly, the noise power standard deviation becomes

$$\sigma_N = \frac{\overline{P_{Z,S}}}{\sqrt{N_{\mathrm{inc}}}}\frac{1}{SNR}. \tag{10}$$

Being signal and noise uncorrelated, the standard deviation σ_S on the estimated useful power is given by the root-mean-square sum

$$\begin{aligned}\sigma_S &= \sqrt{\sigma_R^2+\sigma_N^2}\\ &= \overline{P_{Z,S}}\frac{1}{\sqrt{N_{\mathrm{inc}}}}\sqrt{\left(1+\frac{1}{SNR}\right)^2+\left(\frac{1}{SNR}\right)^2}.\end{aligned} \tag{11}$$

The standard deviation of the height estimation can be simply obtained by translating the power uncertainty to a delay uncertainty. This evaluation has to be performed at the altimetry tracking point of the power reflected waveform model, which corresponds to the zero delay on the simulated power waveforms shown in Fig. 7. If this power to delay uncertainty translation can be locally related to the first derivative of the power waveform ($\overline{P_{Z,S}}'$), the height precision σ_h can be expressed as follows:

$$\begin{aligned}\sigma_h = &\frac{c\overline{P_{Z,S}}}{2\sin\theta_{\mathrm{elev,SP}}\overline{P_{Z,S}}'}\\ &\times\frac{1}{\sqrt{N_{\mathrm{inc}}}}\sqrt{\left(1+\frac{1}{SNR}\right)^2+\left(\frac{1}{SNR}\right)^2}\end{aligned} \tag{12}$$

where $\theta_{\mathrm{elev,SP}}$ is the local elevation angle at the specular point and c is the speed of light in vacuum.

It can be easily noticed from (12) that a large SNR is a necessary but not sufficient condition for guaranteeing high range precision. Indeed, even for infinite SNR, the height precision is still very poor if incoherent averaging is not performed. It is worth noticing that, as shown in (6), the SNR is directly proportional to the cross-correlation integration time T_c and the downlooking antenna gain. If, for example, the downlooking antenna dimension is upper limited by accommodation constraints, the SNR can only be increased with T_c. However, the coherent integration time cannot be increased too much, since this would imply a significant reduction of the available independent waveform samples N_{inc} for incoherent averaging. This is not beneficial since, as can be noticed from (12), the height precision is inversely proportional to $\sqrt{N_{\mathrm{inc}}}$. The optimal design of the instrument which maximizes height precision is then a result of a system analysis which trades the coherent integration time T_c against the down- and uplooking antenna dimensions and the number of incoherently averaged samples. On the other hand, N_{inc} cannot be increased arbitrarily because, otherwise, the spatial resolution would degrade. The number of pulses that can be averaged is limited by the minimum required spatial resolution, which is set to 100 km for mesoscale altimetry. In addition, it can be noticed that the height precision is also inversely proportional to the slope of the power waveform on the tracking point. The waveform slope, in turn, increases with the signal bandwidth. This clearly shows that the interferometric processing maximizes the height precision, since it allows exploiting the full bandwidth of the transmitted GNSS signals.

From these considerations, it appears clear that the knowledge of the cross-correlation statistics is fundamental either for estimating the achievable height precision or for defining the optimum instrument design.

Indeed, the knowledge of the cross-correlation statistics would allow estimating the coherence properties of both the voltage cross-correlation (i.e., $\langle Z(t,\tau)Z^*(t+\tilde{t},\tau+\tilde{\tau})\rangle$) and the power cross-correlation waveforms, i.e., $\langle |Z(t,\tau)|^2|Z(t+\tilde{t},\tau+\tilde{\tau})|^2\rangle$.

The knowledge of the voltage cross-correlation and power cross-correlation coherence would allow estimating the optimum coherent integration time and the corresponding number of independent samples N_{inc}, respectively [30]. A model for the voltage cross-correlation statistics is derived in (79) in Appendix I. Equivalent derivations of (79) can be found in [18] and [28], and validations of the model with experimental aircraft data have also been reported [28]–[30]. In addition, (79) would allow also estimating the lag-to-lag correlation between samples of the same power waveform, which is an important parameter for the design of the optimum delay estimator.

The derivation of the cross-correlation statistics and the consequent system optimization to maximize height precision are not reported in this paper.

A preliminary analysis of the height precision of a space-based PARIS altimeter which exploits the interferometric processing for L1 GPS composite signal is reported in the following, just as an example.

The reference geometry and instrument parameter proposed for PARIS IoD are shown in Table III. The cross-correlation integration time T_c has been set to 1 ms, as a preliminary reference value. For the considered geometry, with 17 s being the time needed for the specular point to travel 100 km over the ocean surface, the number of incoherent average waveform samples is equal to $N_{\mathrm{inc}} = 17\,700$. By adopting (12), the PARIS-IoD height precision results in $\sigma_h = 8$ cm.

An operational PARIS altimeter, featuring down- and uplooking antenna gains of 30 dBi and with an orbit altitude of 1500 km, would achieve a height precision of about 5 cm with 100-km spatial resolution by adopting the L1 GPS composite signal, following the same example case.

The tracks of the reflection points do not repeat, and the scientific exploitation of the data from such operational PARIS mission will have to use the most accurate knowledge of the

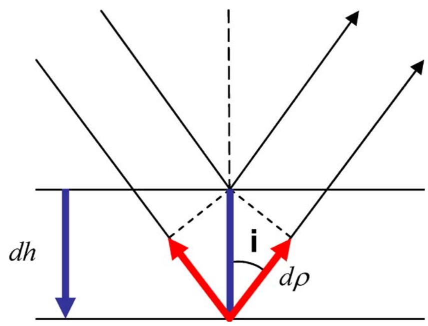

Fig. 9. Range error propagated into height error.

geoid from missions like GOCE as well as tidal models to cope with the varying sampling. The effect of the along-track averaging will also have to be carefully taken into account in the data processing to retrieve the ocean topography at the corresponding spatial resolution.

It is worth mentioning that the presented performance is based on a preliminary estimation and that a further optimization at system level of the instrument processing strategy, front end, and delay estimator would likely guarantee an improvement of the PARIS height precision.

IV. System Design

A. Geometry

Geometry plays an important role in the definition of critical parameters of the PARIS mission such as altimetric accuracy, sampling, and coverage.

On the one hand, the altimetric accuracy degrades with incidence angle for three reasons. First, due purely to geometry, the error in the range measurements $d\rho$ is amplified by the incidence angle i into a height error dh according to (Fig. 9)

$$dh = -\frac{d\rho}{2\cos i}. \tag{13}$$

Second, the slant path across the ionosphere increases with incidence angle, and so do the ionospheric delay and refraction, leading to expectedly larger ionospheric residual errors (Fig. 10). Third, as the downlooking antenna is pointed nadir, its gain reduces with incidence angle, resulting in noisier range observations. For these three reasons, the incidence angle should be minimized.

On the other hand, the number of reflection points (sampling of the ocean surface) and the swath (coverage and revisit time) both increase and improve with incidence angle (Fig. 11). Therefore, there is a tradeoff to be made when deciding on the maximum incidence angle.

A simple approach to such tradeoff has been taken by which the maximum incidence angle is first fixed which guarantees the altimetric performance from an initial orbital height (right part of Fig. 12). Then, the orbital altitude is changed to achieve the required number of reflection points and swath (left part of Fig. 12).

With reference to Fig. 11, the signal transmitted by the GNSS satellite G flying at an altitude H is reflected at S with an

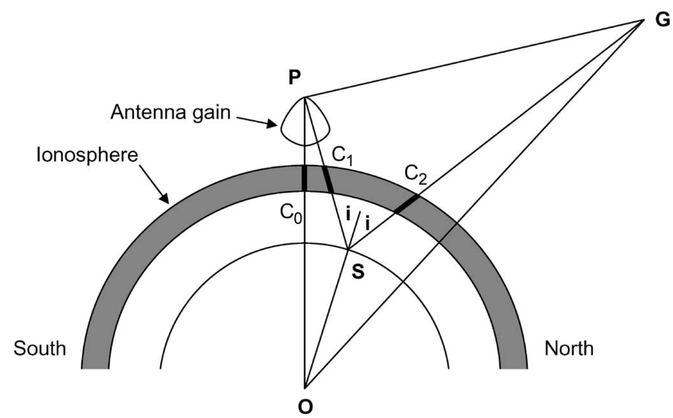

Fig. 10. Ionospheric slant path and antenna gain variation as a function of incidence angle.

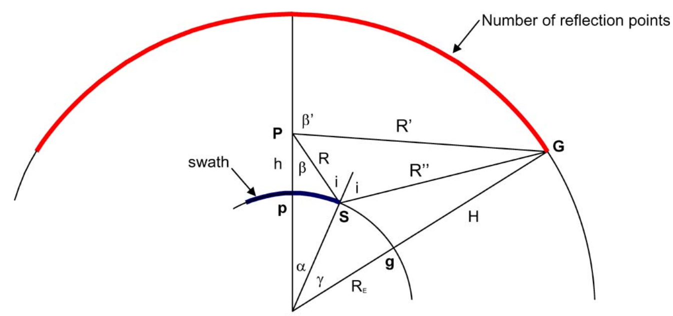

Fig. 11. Number of reflection points and swath as a function of incidence angle.

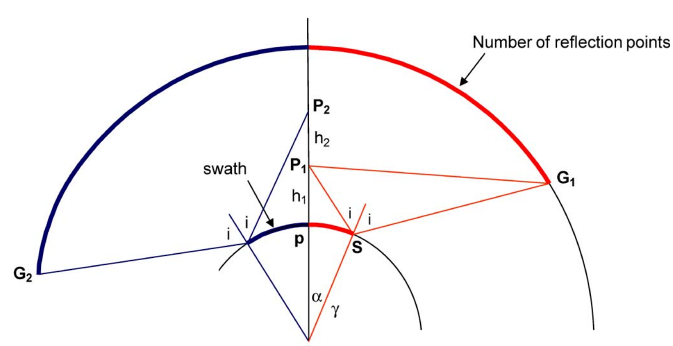

Fig. 12. Geometry solution for PARIS IoD—starting from an initial orbital height h_1, the maximum incidence angle, which guarantees altimetric performance, is first fixed (right part of the figure); then, the orbital height is changed to h_2 in order to achieve the required number of reflection points and swath, maintaining the same maximum incidence angle (left part of the figure).

incidence angle i. The reflected signal is then received by a PARIS altimeter P flying at a height h at a scan angle β, given by

$$\sin\beta = \frac{R_E \sin\alpha}{R} \tag{14}$$

where R_E is the radius of the Earth, α is the angle between the receiver subsatellite point p and the specular point S, as measured from the center of the Earth O

$$\sin\alpha = \frac{R\sin i}{R_E + h} \tag{15}$$

and R is the distance from the PARIS altimeter to the specular point, i.e.,

$$R = \sqrt{R_E^2\cos^2 i + 2hR_E + h^2} - R_E\cos i. \tag{16}$$

The swath is proportional to angle α

$$2 \times \overline{pS} = 2\alpha R_E \tag{17}$$

and the number of reflection points is proportional to $\alpha + \gamma$, where γ is the angle between the specular point S and the transmitter subsatellite point g, i.e.,

$$\cos^2\gamma + b\cos\gamma + c = 0 \tag{18}$$

with

$$b = -2\frac{R_E\sin^2 i}{R_E + H} \tag{19}$$

$$c = \frac{R_E^2\sin^2 i}{(R_E+H)^2} - \cos^2 i. \tag{20}$$

The spherical cap defined by the angle $\alpha + \gamma$ about the zenith of the PARIS satellite subtends a solid angle of

$$\Omega = 2\pi\left[1 - \cos(\alpha+\gamma)\right] \tag{21}$$

which provides an average number of reflection points n equal to

$$n = \frac{\Omega}{4\pi\sin I}N = \frac{1-\cos(\alpha+\gamma)}{2\sin I}N \tag{22}$$

with N being the number of GNSS satellites and I as their orbital inclination.

The direct signal is received by the uplooking antenna at a scan angle β'

$$\sin\beta' = \frac{R_E + H}{R'}\sin(\alpha+\gamma) \tag{23}$$

where R' is the distance between the two satellites P and G

$$R'^2 = (R_E+h)^2 + (R_E+H)^2 - 2(R_E+h)(R_E+H)\cos(\alpha+\gamma). \tag{24}$$

Clearly, the scan angle of the uplooking antenna is larger than that of the downlooking antenna. However, the pattern requirements for the downlooking beam in terms of gain and sidelobes will be generally more severe than those for the uplooking antenna, and the scan angle of the downlooking antenna will be the one driving the design of the antenna (as both arrays are built identical).

Two cases are presented in Table V corresponding to maximum incidence angles of $i = 35^\circ$ and $i = 40^\circ$. The scan angle of the downlooking antenna is smaller in the first case, and for the highest orbital altitude of 1500 km, it takes a value of 27.7°. The corresponding number of reflection points is 17, assuming five GNSS constellations, spread over a swath of about 1600 km. The distance between the reflection point tracks over the ocean is thus expected to be around 100 km on average. The size of the swath allows for a revisit time of two days.

The maximum incidence angle could be increased to 40° for the same orbital height of 1500 km, leading to 22 reflection points, but in this case, the scan angle of the downlooking antenna would have to be increased up to 31.3°, which can be critical for the design of the antenna.

Overall, Table V presents an envelope of orbital altitudes and incidence angles where it is believed that both an operational mission and the PARIS-IoD mission could very well fall in.

The following is a final remark on the knowledge of the horizontal position of the reflection points. Assuming an ellipsoidal Earth and no uncertainty in the delay observations, the error in the horizontal positioning of the specular point is negligible [44]. If, in addition, a deflection of the vertical of the geoid of 10–5 rad is considered, then the horizontal error increases to about 10 m for a 1000-km orbital altitude. If the reflection point is calculated over the GOCE geoid (or an homothetic surface to the geoid), then the error should greatly reduce. The impact of this horizontal uncertainty in the altimetry accuracy should also be negligible.

B. *Instrument Design*

The instrument of a PARIS operational mission would be designed to receive any of the frequency bands of any of the GNSS systems (namely, the U.S. GPS, the European GALILEO, the Russian GLONASS, the Chinese COMPASS, and the Indian INSS) as well as the signals of their satellite-based augmentation systems (geostationary satellites transmitting navigation signals) of the mentioned GNSS constellations and, finally, the signals from any regional constellation such as the Japanese QSZZ. This paper will focus, however, in the simpler design of the instrument proposed for the PARIS IoD.

The proposed antenna of the PARIS IoD consists of two identical phased arrays (except for the polarization), mounted back-to-back, with the front-end electronics housed in between them. The uplooking array is right-hand circularly polarized, whereas the downlooking array has left-hand circular polarization. This antenna allows generating and steering four parallel uplooking and four parallel downlooking high-gain beams. The uplooking beams are steered toward four transmitting satellites, each one being either GPS or GALILEO. The downlooking beams are supposed to track the corresponding reflection points over the ocean or, in general, over the Earth surface.

The number of elements in each array is mainly driven by the minimum SNR to be achieved in the reception of the reflected signals. As mentioned in the interferometric processing section earlier, an antenna gain of about 23 dBi is required for a PARIS IoD flying around a 500-km altitude to demonstrate mesoscale altimetry. Such gain can be achieved by a hexagonal array of 1.1 m consisting of 31 elements, each having a directivity of 8 dB, such as the one in Fig. 13. These elements would be designed to receive the lowest and highest navigation bands (currently L1-E1 and L5-E5a, respectively, in the case of GPS and Galileo) for best estimation of the ionospheric delay. The field of view of each element would be typically between 25°

TABLE V

AVERAGE NUMBER OF REFLECTION POINTS, SWATH, AND SCAN ANGLES β AND β' OF THE DOWN- AND UPLOOKING ANTENNAS, RESPECTIVELY, AS A FUNCTION OF ORBITAL ALTITUDE FOR A MAXIMUM INCIDENCE ANGLE OF $i = 35°$ AND $i = 40°$. FIVE GNSS CONSTELLATIONS OF $30 + 3$ SATELLITES HAVE BEEN ASSUMED: GPS, GLONASS, GALILEO, COMPASS, AND INSS

i=35°

h	H	R	α	γ	α+γ	Number of reflections	Swath	β	β'
Km	Km	Km	deg	deg	deg		Km	deg	deg
500	20200	600	2.9	27.1	30.0	13	638	32.1	39.4
750	20200	893	4.1	27.1	31.2	14	917	30.9	41.4
1000	20200	1183	5.3	27.1	32.4	15	1174	29.7	43.4
1250	20200	1469	6.4	27.1	33.5	16	1411	28.6	45.2
1500	20200	1752	7.3	27.1	34.4	17	1631	27.7	46.9

i=40°

h	H	R	α	γ	α+γ	Number of reflections	Swath	β	β'
Km	Km	Km	deg	deg	deg		Km	deg	deg
500	20200	637	3.4	31.1	34.6	17	759	36.6	45.1
750	20200	945	4.9	31.1	36.0	18	1088	35.1	47.4
1000	20200	1248	6.3	31.1	37.4	20	1389	33.7	49.6
1250	20200	1547	7.5	31.1	38.6	21	1667	32.5	51.6
1500	20200	1841	8.7	31.1	39.8	22	1923	31.3	53.6

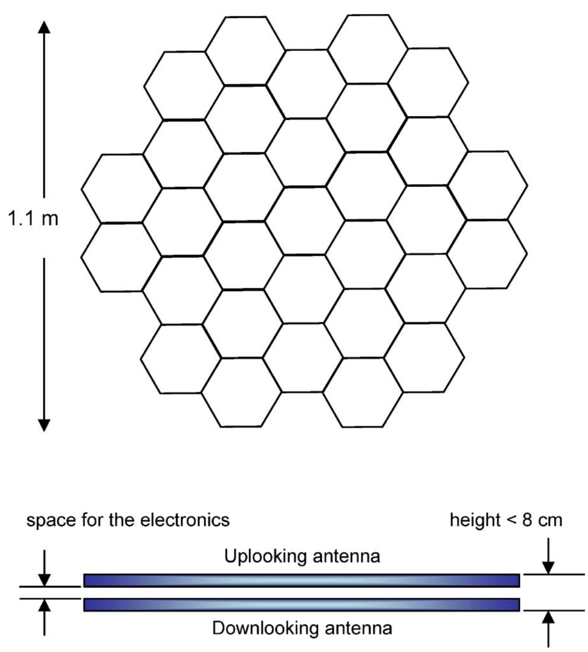

Fig. 13. Back-to-back double phased array antenna.

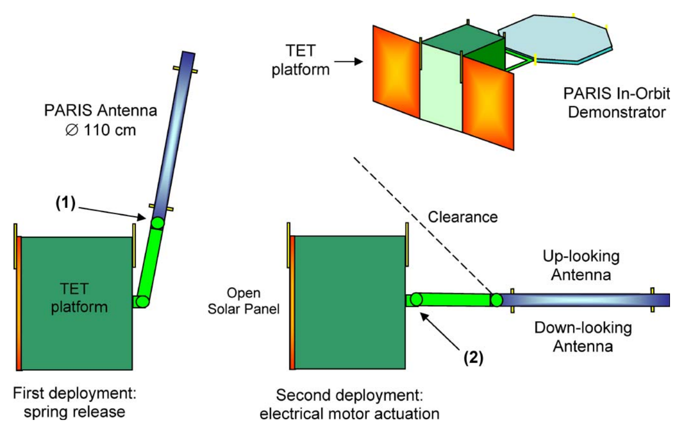

Fig. 14. Accommodation and deployment of the PARIS antenna on the small German TET platform.

and 35° about boresight to ensure coverage while preserving altimetric performance.

Fig. 14 shows one possible solution to accommodate such an antenna on top of a small platform like the German total electron content (TET) platform. The antenna would sit on top with four hold-down and release mechanisms, being launched inside the interface cone to a main satellite passenger using a Rockot launcher, for example (Fig. 3). The antenna would open in two stages, first using a spring-loaded mechanism and second with an electrical motor. The deployed antenna configuration would ensure clearance in both the upper and lower hemispheres to receive direct and reflected GNSS signals.

The proposed back-to-back mechanical arrangement of the two identical up- and downlooking phased arrays serves various purposes. On the one hand, the phase centers of both antennas are in close proximity to one another (less than 10 cm as a goal, as shown in Fig. 13), thus minimizing their impact on the altimetry performance. On the other hand, such an arrangement allows a compact layout of the front-end electronics in between the two arrays, as shown in Fig. 15, in which every uplooking element is paired up with one downlooking element.

The major advantage of such a paired-element layout is that both the direct and reflected signals can be easily routed via pressure connectors from each antenna array element to a calibration switch circuit inserted between them and their low noise amplifiers (LNAs). The calibration switch circuit allows accurate delay and amplitude calibration. This feature is essential to achieve the scientific goals of the PARIS IoD.

Fig. 16 shows the high-level architecture of the beamformers. Each up- and downlooking antenna elements of the same pair are both connected to the same front end consisting of the calibration switch and an LNA. After low-noise amplification, the signals enter the beamformers proper. There are two identical beamformers, labeled A and B in Fig. 16, each connected to one of the two arrays.

Each beamformer first splits the signals coming out from each of the M antenna elements ($\mathrm{UP}_1, \ldots, \mathrm{UP}_M$ or

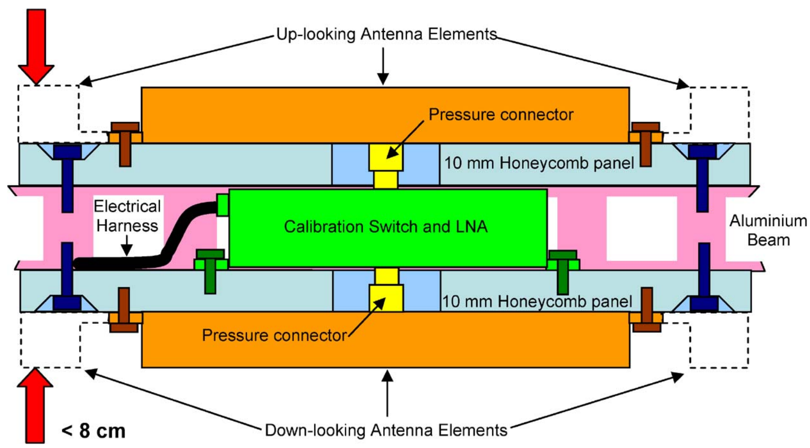

Fig. 15. Cross section of the PARIS antenna sandwich showing the element pairing through the calibration switch and LNA front-end electronics.

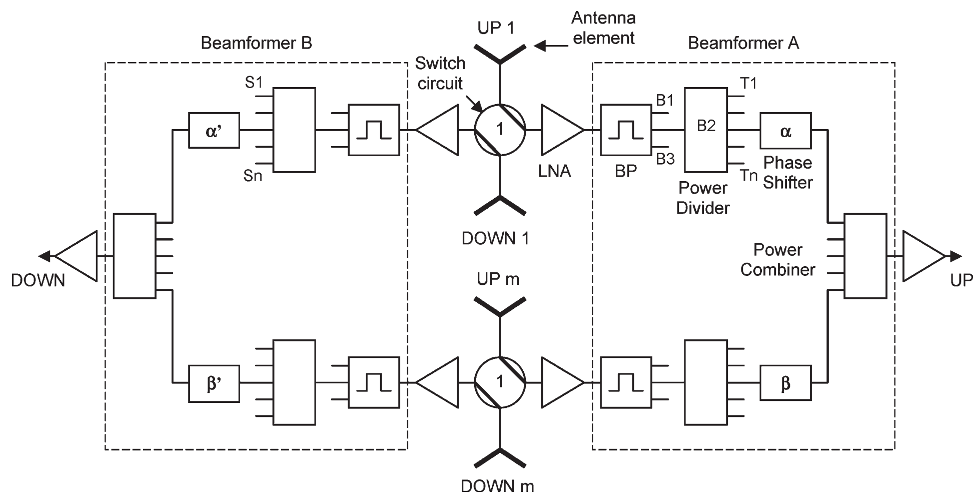

Fig. 16. Beamformer high-level architecture, including up- and downlooking arrays as well as calibration switch and LNAs. The calibration switch is in position 1.

$\mathrm{DOWN}_1, \ldots, \mathrm{DOWN}_M$ in Fig. 16) into their several frequency bands using bandpass filters (BPFs). This is necessary because the frequency separation between navigation bands is large enough to require independent beam steering for each frequency. As mentioned earlier, the PARIS IoD would only use two bands: the currently upper (GPS L1 and GALILEO E1) and lower (GPS L5 and GALILEO E5) navigation bands.

The signal of each antenna element and each GNSS frequency band is then split into N branches using power splitters, with $N = 4$ being the number of GNSS transmitting satellites to be tracked (T1, ..., TN) as well as the number of corresponding specular points (S1, ..., SN). This results in $M \times N$ signals inside each beamformer per antenna element and frequency band. Then, M signals (one output taken from each of the M power splitters) of each of N sets are properly phase shifted using phase shifters before getting combined by means of a power combiner, this resulting in one high-gain beam. There are $N = 4$ power combiners in each beamformer and for each GNSS band, resulting in N parallel high-gain beams per frequency and array. All these beams are needed to track four GNSS satellites and their four specular points at two frequencies.

The values to be applied to the phase shifters are calculated and continuously refreshed on-the-fly by the instrument computer. For this purpose, the orbital parameters of the GPS and GALILEO satellites have to be uplinked from ground, and the current time, position, velocity, and attitude information of the PARIS satellite itself are to be provided to the instrument computer by the navigation receiver onboard the TET platform. The uplink of the GPS and GALILEO ephemeris would be done using the S-band uplink from ground to the TET platform, which would pass this information onto the PARIS altimeter payload computer.

Every pair of direct and reflected signals belonging to the same GNSS satellite and navigation band is processed as explained earlier: They are first matched in Doppler frequency and delay and then complex cross-correlated. It is important to note that, as GNSS pseudorandom signals are not stationary processes, the complex correlation has to be implemented in full, i.e., using all four products resulting from the combination of real and imaginary parts of the two intervening signals.

The match in Doppler frequency has to ensure that, during the coherent integration time over which the complex cross-correlations are computed, the relative phase between the direct and reflected signals remains quite constant. The match in delay has to keep the cross-correlation delay window adequately centered on the delay of the specular point. The values of the

Doppler and delay shifts, as well as the times at which they are applied, have to be accurately recorded since they are needed by the altimetric processor on ground.

In addition to the cross-correlation between the direct and reflected signals, the PARIS altimeter is able to measure the autocorrelation of the direct signal. The purpose of this is to provide such ACF to the ground processor for optimum retracking of the specular reflection point. The refresh rate at which such ACF would have to be updated is a matter of future research, but it is probably a slow-time-varying function, linked to thermal variations on both the PARIS as well as the GNSS satellite.

Subject to a future optimization that would take into account the intersample cross-correlation properties, the required delay resolution of the correlator T is driven by the bandwidth of the GNSS signals B. Taking a factor 2 margin over the Nyquist limit, this leads typically to delay resolutions of

$$T = \frac{c}{4B} \tag{25}$$

which translates into 0.83 m for GALILEO E5 or GPS L5 and 1.66 m for GALILEO E1 or GPS L1. The corresponding sampling rates are 540 and 270 Msamples/s, respectively. The delay window of the waveforms may be typically of 60 m, comprising 72 or 36 delay samples per waveform. Assuming a coherent integration time of 2 ms and 16-b correlations, the data rate at the correlator output for all four specular points and the two frequencies will be about 7 Mb/s. These waveforms can be further incoherently accumulated onboard to reduce data throughput. An incoherent integration of 100 waveforms, which corresponds to a 0.2-s observation time (about 1.1 km on the ocean surface), would lead to a 70-kb/s instrument output data rate. This is compatible with a mass memory of less than 5 Gb and an X-band downlink of less than 10 Mb/s.

C. Onboard Calibration

To enable the exploration of scientific applications of GNSS reflected signals, it is crucial to provide well-calibrated observations, both in delay and in amplitude. The back-to-back double phased array of the PARIS IoD is thought precisely to facilitate calibration.

Internal delays within the electronics of the PARIS altimeter are removed by swapping arrays and receive chains and averaging the measured delays of the specular point in the two swapped configurations. The swapping is achieved by means of the switch circuit in the front end, accompanied by a change in sign in the Doppler shift coming out of the NCO and in the delay shift right after digitalization, i.e., after the A/D converter in Fig. 4.

With reference to the detailed block diagram of the front end and the beamformer in Fig. 16, when the switch circuit is in position 1, the following signals are formed for the up- and downlooking links of a specific GNSS satellite:

$$x(t) = x_1(t-a-\alpha-e) + \cdots + x_m(t-b-\beta-e) \tag{26}$$

$$y(t) = y_1(t-a'-\alpha'-e') + \cdots + y_m(t-b'-\beta'-e') \tag{27}$$

where

- a and b total delays due to the LNA, BPF, power divider, and power combiner for elements 1 and m of beamformer A, respectively;
- a' and b' corresponding total delays for beamformer B;
- α and β delays of the phase shifters for elements 1 and m of beamformer A, respectively;
- α' and β' corresponding phase shifter delays for beamformer B;
- e and e' total delays due to the rest of the receiving chain beyond the output of the beamformer and up to the input of the correlator.

The average delay between the direct and reflected signals is

$$\tau_1 = \frac{1}{M}(a - a' + \alpha - \alpha' + \cdot + b - b' + \beta - \beta') + (e - e'). \tag{28}$$

Similarly, when the switch circuit is in position 2, as shown in Fig. 17, the signals become

$$x(t) = x_1(t-a'-\alpha'-e') + \cdots + x_m(t-b'-\beta'-e') \tag{29}$$

$$y(t) = y_1(t-a-\alpha-e) + \cdots + y_m(t-b-\beta-e) \tag{30}$$

and the average delay

$$\tau_2 = -\frac{1}{M}(a - a' + \alpha' - \alpha + \cdots + b - b' + \beta' - \beta) - (e - e'). \tag{31}$$

If delay observations are made in the two configurations and then averaged, the residual internal receiver delay error is obtained

$$\tau = \frac{\tau_1 + \tau_2}{2} = \frac{1}{M}(\alpha - \alpha' + \cdots + \beta - \beta'). \tag{32}$$

This is the average differential delay of the phase shifters when they are set to the two values corresponding to the GNSS satellite and the specular reflection of its signal. Both values are close to each other (from the scan angles of Table V, typically within 20°), and therefore, the residual internal delay after the proposed calibration is likely to be very small. Nevertheless, the proposed technique can be further improved if the lookup tables of differential delays of the phase shifters are available from ground characterization tests.

It should be noted that, when the switch circuit is in position 1, the Doppler and time shifts are applied as shown in the general block diagram in Fig. 4. These shifts must be applied with the inverted sign when the switch circuit is in position 2.

The update rate of the delay calibration can be low, as delays change only slowly in orbit due to thermal variations. As an example, the instrument delays could be obtained a few times per orbit using the average difference

$$\tau_o = \frac{\tau_1 - \tau_2}{2} = \frac{1}{M}(a - a' + \cdots + b - b') + (e - e') \tag{33}$$

and transmitted to ground for correction by the altimetric ground processor.

Well-established microwave radiometer techniques are proposed to calibrate accurately the amplitude of the waveforms

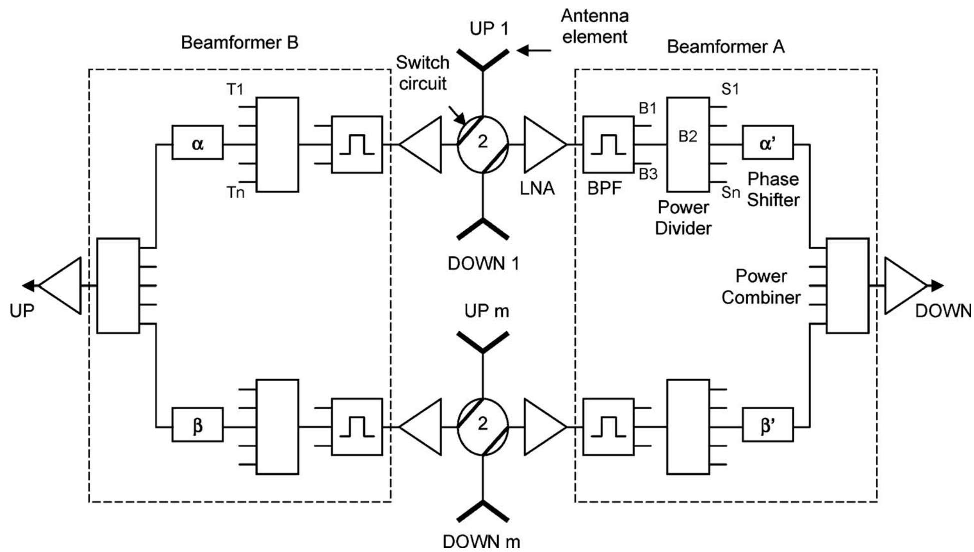

Fig. 17. Position 2 of calibration switch during delay calibration.

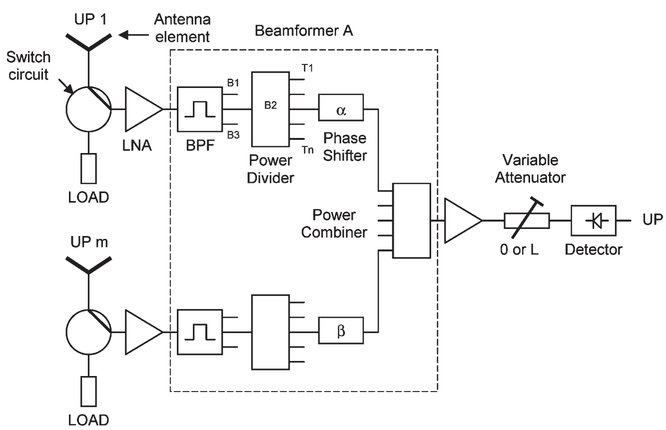

Fig. 18. Amplitude calibration based on radiometric techniques.

generated by the PARIS altimeter. The basic underlying method is called the four-point technique [39] and consists of measuring the cold sky and an internal load sequentially, both with and without an attenuator in the IF stage of the receiver chain (Fig. 18). From the four output power levels of the four combinations, it is possible to derive very precisely the gain, offset, and noise figure of the receiving chains.

The first two steps of the four-point method are performed measuring the output power when the uplooking array is in view of the cold sky, which is the nominal scenario. The switch circuit connects the antenna elements to the LNAs. To view the cold sky, the beams have to be steered away from the GNSS satellites, using the information from the computer. Access to cold sky is assured by the fact that the orbital inclination of current GNSS systems (55° in GPS, 56° in GALILEO, 64.8° in GLONASS, and 55.5° in COMPASS) leaves a minimum angle of 25° around the Earth rotation axis empty of satellites. The output power is measured by a detector branched in the IF section of the receiver, right at the input of the A/D converter in the block diagram of Fig. 4. Before the detector, there is a variable attenuator which can take a value of 0 (no attenuation) or L (typically some 6–9 dB). Two power measurements of the cold sky are taken at each of the two attenuation values.

The final two steps of the four-point technique are accomplished when a load is presented at the input of all receivers. This is achieved when the front-end switches connect the internal loads to the LNAs, which is equivalent to placing a microwave absorber at the physical temperature of the loads in front of the antenna [40]. The physical temperature of the loads must therefore be monitored using thermistors. As with the cold sky, two output power levels are measured with the internal loads connected at the input to the receivers for the two values of the IF attenuator, i.e., 0 and L.

From the four output power levels (cold sky and internal load, for 0 and L attenuation), the overall gain, offset, and receiver noise of each uplooking high-gain beam of beamformer A can be derived.

The calibration of the downlooking beams can be obtained either by rotating the satellite upside down or by switching beamformer B to the uplooking array. The former is the most accurate method as it includes the nominally downlooking antenna itself. A possible implementation of the proposed technique would consist of turning the satellite once a month, for example, to calibrate the downlooking beams and, in addition, to perform the amplitude calibration a couple of times per orbit in combination with the delay calibration (where beamformer B is swapped to the uplooking array).

Both delay and amplitude calibration are enabled by the back-to-back double phased array configuration in Fig. 15, in combination with the switch circuit shown in Fig. 19. This switch circuit allows the swapping to remove instrumental delays as well as the connection to the internal loads for amplitude calibration.

D. Intersatellite Interference

The interferometric technique proposed for the PARIS IoD assumes that there is only one GNSS satellite at any time inside the uplooking beam and only one reflected signal in the downlooking beam. In this section, this assumption is verified.

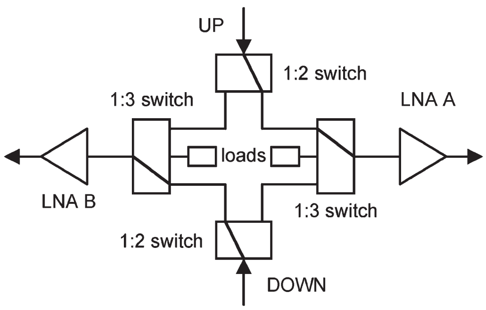

Fig. 19. Calibration switch enabling delay and amplitude calibration.

The average solid angle $d\Omega$ available for each GNSS satellite is

$$d\Omega = \frac{4\pi \sin I}{N} \tag{34}$$

while the beamwidth of the antenna is given by its gain G

$$\Omega_o = \frac{4\pi}{G}. \tag{35}$$

The ratio between the two solid angles above yields the expected number of GNSS satellites inside the main beam of the antenna

$$m = \frac{\Omega_o}{d\Omega} = \frac{N}{G \sin I}. \tag{36}$$

Taking $G = 23$ dB, $I = 55°$, and $N = 150$ (5 GNSS constellations of 30 satellites each), the ratio above gives $m = 0.91$. This ratio is less than one, meaning that, assuming an evenly spatial distribution of GNSS satellites, there will be only one GNSS satellite in the up- and downlooking beams. A larger antenna gain, as the one expected for an operational mission, will lead to an even smaller ratio, ensuring the presence of only one satellite per beam.

However, neither the GNSS satellites will be evenly distributed in space nor the antenna beam will have infinite rejection to signals coming through the roll-off of the antenna main beam or through its sidelobes. Therefore, it should be expected that more than one GNSS signal can be received through each of the uplooking beams (and, similarly, through the downlooking beams). When this happens, some intersatellite interference will occur.

The ranges of delays (difference between maximum and minimum possible delays) for any GNSS satellite are about 700 and 300 km for PARIS orbital heights of 1500 and 750 km, respectively (Table VI). Clearly, the higher the PARIS orbit, the larger the delay range. Assuming a negligible effect from a waveform 30 km away in delay (spatially, this represents a distance of at least 150–250 km on the ocean surface), this yields 23 and 10 independent delay bins, for the two orbital altitudes.

The range of Doppler shift (difference between maximum and minimum possible Doppler frequencies) for any GNSS satellite depends mostly on the orbital altitude of the PARIS satellite. The Doppler ranges are 27 and 32 kHz for 1500- and 750-km PARIS orbital heights, respectively. Assuming a coherent integration time of 0.5 ms, this leads to 13 or 16 independent Doppler bins.

In total, there are $23 \times 13 = 299$ or $10 \times 16 = 160$ delay–Doppler bins for a number of reflection points between $n = 22$ and 14 (Table V). Because the number of bins is much higher than the number of reflection points, the intersatellite interference will happen only seldom. Furthermore, when it happens, it will likely last only for a short period of time when antenna gain, delay, and Doppler shift are all contributing. Intersatellite interference is predictable and hence can be handled adequately. Nonetheless, it is a subject to account for carefully in the system design of a PARIS altimeter.

V. Ionospheric Correction

The basic observable for the system is the single path delay difference in delay between the direct and the reflected paths

$$\rho = -2h \cos i + I + T + L \tag{37}$$

where h is the altitude, i is the incidence angle, I and T are the slant ionospheric and tropospheric delays, respectively, and L is the instrumental delay. Fig. 10 shows the geometry of such configuration with an incident angle of 30°.

The ionosphere is an ionized part of the Earth atmosphere lying between roughly 50 km up to several thousand kilometers, characterized by a spatially and temporally variable refractive index which depends on the electronic density in the region under consideration. This refractive index results, in turn, in an additional group delay (or, equivalently, a phase advance of the same magnitude) when integrated over the part of the ray intersecting the ionosphere. As a consequence, the path delay difference between the direct and the reflected rays is biased by a spatiotemporally variable amount linked to the ionospheric state. This delay is frequency dependent, and its first-order relation is given by

$$I(f) = \frac{40.3}{f^2} \cdot \int\limits_{\text{path}} N \cdot dl = \frac{40.3}{f^2} \cdot sTEC = \frac{1}{f^2} I' \tag{38}$$

where I is the group delay error (in meters), f is the frequency (in hertz), N is the electron density (electrons per cubic meter), $sTEC$ is the slant total electron content (electrons per square meter), $I' \equiv 40.3 \times sTEC$, and *path*, in this case, is the difference of the propagation paths between direct and reflected contributions. The $sTEC$ may also be expressed in TECU (TEC units), where 1 TECU $= 10^{16}$ electrons/m^2. At the L1 frequency (1575.42 MHz), the delay is approximately 16 cm for 1 TECU. The distribution of electron density (and, therefore, of TEC) depends on different factors such as time of the day, location, season, solar activity (which is related to the epoch within the solar cycle), or level of disturbance of the ionosphere, such as those due to geomagnetic storms.

Higher order ionospheric terms, varying with $1/f^3$, $1/f^4$, etc., depend not only on electron density but also on other factors such as geomagnetic field and different paths due to dispersive refraction [41], [42]. In general, the contribution of those terms is relatively low, but worst case values at L-band

TABLE VI
RANGE OF DELAYS FOR THREE GNSS CONSTELLATIONS (GPS, GALILEO, AND GLONASS) TO STUDY INTERSATELLITE INTERFERENCE (REFER TO FIG. 11 FOR THE NOMENCLATURE)

h=1500 Km

GNSS	i	H	R	R''	R'	τ = R+R''–R'	Δτ
	degrees	Km	Km	Km	Km	Km	Km
GPS	0	20200	1500	20200	18700	3000	714
	35	20200	1752	21099	20566	2286	
GALILEO	0	23200	1500	23200	21700	3000	706
	35	23200	1752	24125	23583	2294	
GLONASS	0	19100	1500	19100	17600	3000	718
	35	19100	1752	19988	19458	2282	

h=750 Km

GNSS	i	H	R	R''	R'	τ = R+R''–R'	Δτ
	degrees	Km	Km	Km	Km	Km	Km
GPS	0	20200	750	20200	19450	1500	318
	35	20200	893	21099	20810	1182	
GALILEO	0	23200	750	23200	22450	1500	316
	35	23200	893	24125	23834	1184	
GLONASS	0	19100	750	19100	18350	1500	319
	35	19100	893	19988	19700	1181	

can reach up to 10 cm with residual errors on ionospheric free combinations of the same order of magnitude. They will not be considered on this preliminary performance assessment due to the limitations on the reduced high sampling data sets available. Other important ionospheric effects at L-band are amplitude and phase scintillations, which are rapid fluctuations of amplitude and phase of the radiowave signal caused by small-scale irregularities which modify the ionospheric refractive index. They will not be considered for the current analysis due to the fact that they are localized effects that may reduce the availability (number of samples) of the observables during some disturbed periods, particularly around the geomagnetic equator, but they are not expected to have a major impact on accuracy.

In PARIS, the direct path crosses only a very thin part of the ionosphere and plasmasphere, the reflected path crosses twice its heavily ionized F-layer, and both paths are included in the I' term.

In (37), the nondispersive tropospheric delay affects only the reflected path (twice), and it can be removed with double differencing (difference of reflected-minus-direct delay observations at two positions—mesoscale processing) for short ground baselines, where the paths that crossed through the troposphere can be considered homogeneous, or, otherwise, on postprocessing using correction models assimilated by ground meteorological observations to improve accuracy. On the other hand, most internal biases are eliminated by calibration, with the technique explained earlier, and by the differencing process; therefore, residual internal biases are expected to be negligible.

A. Multifrequency Observations

Assuming that all the other sources of error are taken into account, one possible way of estimating the ionospheric delay is to rely on multifrequency observations. Indeed, the refractive index of the ionosphere is frequency dependent [see (38)], and measuring the delay at two different frequencies can resolve the delay bias. This is the usual technique applied to obtain an ionospheric free solution from GNSS systems [43].

In practice, however, the present GNSS systems (as GPS) transmit high-rate open-access codes only in L5, but not at L1. If the L1 C/A code were used for the ionospheric correction, then the higher precision of the L5 code would not be usable, and its advantages for altimetry would be lost. Fortunately, GPS (another future GNSS systems as GALILEO) will transmit in the future several signals with different rates at three different frequencies. With the current limitations of the C/A code, a solution to increase precision is by doing the proposed interferometric processing by cross-correlation of all the received signals in the whole bandwidth of both L1 and L5 with the reflected signal.

As an example, assuming that PARIS is using L1 and L5 signals, the single-difference observable equations for each carrier frequency are, respectively

$$\rho_1 = -2h\cos i + \frac{I'}{f_1^2} \tag{39}$$

$$\rho_5 = -2h\cos i + \frac{I'}{f_5^2}. \tag{40}$$

Solving this system of equations results in a single-difference height of

$$h_{15} = 1.26\frac{\rho_5}{2\cos i} - 2.26\frac{\rho_1}{2\cos i}. \tag{41}$$

Assuming that the accuracy on slant pseudoranges is similar at both frequencies, the altimetric accuracy after ionospheric correction becomes

$$\sigma_{h_{15}} \approx 2.59\,\sigma_{h,0} \tag{42}$$

where $\sigma_{h,0}$ is the single-frequency altimetric accuracy in the ideal case where no ionosphere is present. Similarly, it is also possible to estimate the ionospheric delays at L1 and L5 with the following accuracies:

$$\frac{1}{f_1^2}\sigma_{I_1} = 1.78\ \sigma_{h,0} \tag{43}$$

$$\frac{1}{f_5^2}\sigma_{I_5} = 3.20\ \sigma_{h,0}. \tag{44}$$

These results show that, with this ionospheric correction technique, one cannot take advantage of the high-rate codes in the lower GNSS frequency bands because most of the error amplification is driven by the precision in the upper band. This is very relevant in the case of GALILEO where high-rate signals are to be transmitted in the lower band.

B. Spatial Filtering

To circumvent this problem, one can use the fact that the ocean altimetric signal and the ionospheric delay are uncorrelated, and make the reasonable assumption that the ionospheric spatial variability is limited over short spatial scales. In that case, improved estimations of this large-scale ionospheric delay can be done through a regression over N successive measurement points ($N = 3$ for linear regression and $N = 5$ for a fourth-order regression). If the regression were perfect, then the accuracy of the estimation of the ionospheric delay over this larger scale would be improved by a factor $\sqrt{N}$. Using these optimized ionospheric delays leads to a final altimetric accuracy given by (see Appendix III)

$$\sigma_h = \sqrt{\frac{1}{2} + \frac{1.78^2}{4N} + \frac{3.20^2}{4N}}\ \sigma_{h,0} \tag{45}$$

hence $\sigma_h \approx 1.27\ \sigma_{h,0}$ for $N = 3$ and $\sigma_h \approx 1.08\ \sigma_{h,0}$ for $N = 5$. The degradation caused by the ionospheric correction is considerably limited.

This approach relies on two main assumptions: 1) The ionospheric delay signal I' is varying smoothly as the PARIS satellite progresses along its orbit, and/or 2) it is possible to apply an efficient regression according to the predictability of the ionospheric variations.

In an operational mission, observations at a third GNSS frequency band such as GPS L2 or GALILEO E2 could be added, in which case (45) turns into (Appendix II)

$$\sigma_h = \sqrt{\frac{1}{3} + \frac{1.68^2}{9N} + \frac{2.76^2}{9N} + \frac{3^2}{9N}}\ \sigma_{h,0} \tag{46}$$

leading to $\sigma_h \approx 1.03\ \sigma_{h,0}$ for $N = 3$ and $\sigma_h \approx 0.87\ \sigma_{h,0}$ for $N = 5$.

C. Simulation Results

To evaluate the performance of such an approach, one needs to simulate the variation of the ionospheric delay, based on a realistic description of the total electron content (TEC). Here, the TEC product of the dual-frequency radar altimeter RA-2 onboard Envisat has been used. The TEC is the vertically

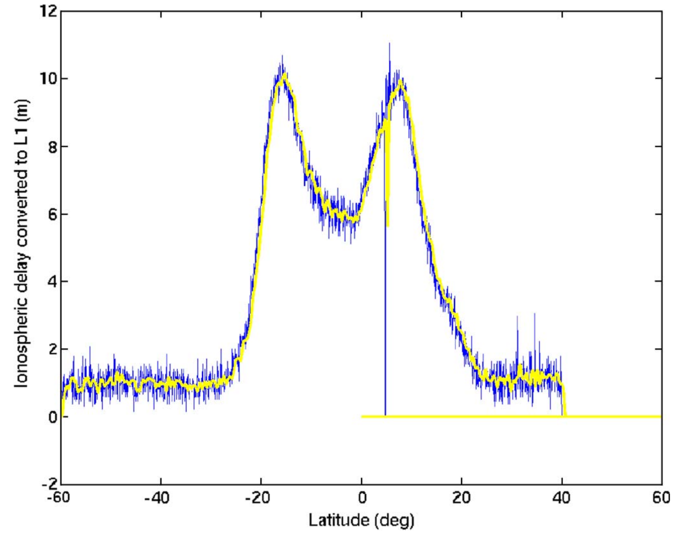

Fig. 20. Vertical TEC measured by RA-2 radar altimeter, converted into equivalent L1 delay (m). Descending orbit, May 6, 2004. (Dark line) Raw data. (Light line) Filtered data.

integrated electron density collected for given spatiotemporal coordinates. The dual-frequency approach has commonly been used to correct the ionospheric delay in classical altimetry observations, and the TEC along the orbit is a natural by-product of such measurements (collected at S- and Ku-bands in the case of RA-2). Two half orbits were selected for this study, one ascending (10 pm local time) and one descending (10 am), both on May 6, 2004. We have focused our description on the worst case which is the evening orbit.

The TEC observations from the dual-frequency altimeters are also subject to retrieval errors. These errors come from instrument noise as well as from limitations in the retrieval approach. One example of the latter is the fluctuation in the backscattered response of the surface. To limit its impact, altimetric observations over land and sea ice are first discarded. Then, a filtering process similar to the one described in [36] is applied to the TEC data, where one tries to separate the smaller scale fluctuations of the ionosphere along the orbit from the residual instrument and algorithm noise. Fig. 20 shows the results of such a filtering.

Starting from these TEC data, the double difference is computed for a worst case scenario, i.e., the case where one reflection point is at nadir and the other one is ahead along track with an incidence angle of 35°. The longer path through the ionosphere is taken into account for the second reflection point, but for simplification purposes, the ionospheric delay is concentrated at a height of 400 km. It is also worth noting that, for this geometric configuration, two different segments of the ionosphere are crossed by the $i = 35°$ reflection path (points C_1 and C_2 in Fig. 10, around 556 and 1118 km ahead of C_0 at 400-km altitude).

For this scenario, the "ionospheric mesoscale delay" (the double-difference ionospheric delay) and the residual delay are computed along the half orbit. The results are shown in Fig. 21. The "ionospheric mesoscale delay" is the output of the double-differencing algorithm applied for the geometry described earlier to each point along the orbit. The "residual

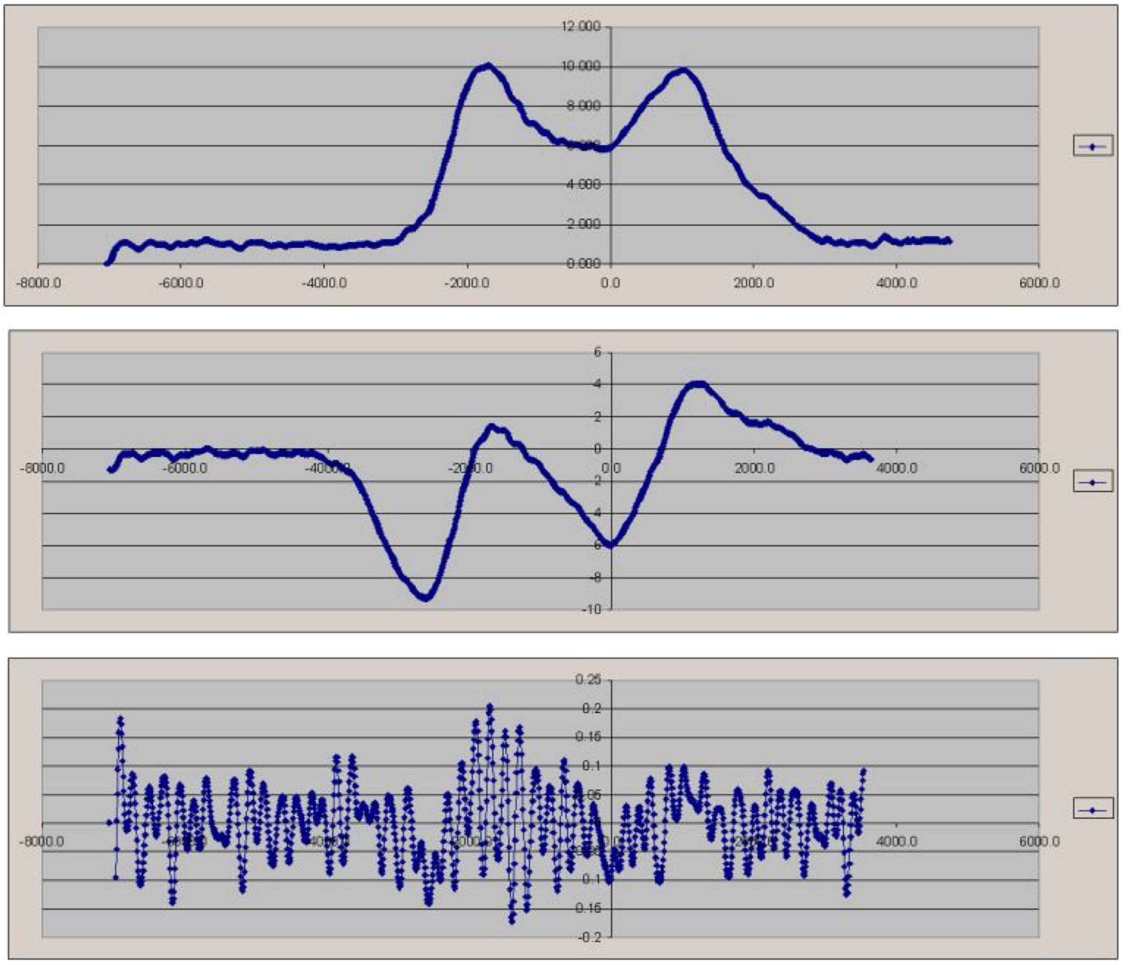

Fig. 21. Output of the double-difference processing. (Top) RA-2 derived L1 delay (m). (Middle) Worst case double-difference ionospheric delay (m). (Bottom) Double-difference ionospheric delay residual after subtracting a 200-km smoothing filter to middle plot (m).

delay" is generated by substracting to the "ionospheric mesoscale delay" its smoothed value obtained through the use of a 200-km sliding average window (hence representing the output of a linear regression algorithm).

The resulting root-mean-square error of the residual delay is approximately 6.5 cm (bottom plot in Fig. 21), and this value will be taken as the ionospheric contribution to the error budget. Considering that the residual error is proportional to the absolute ionospheric electron density, the analyzed data set has an electron density which is above 75th percentile of the absolute electron density providing above one-sigma confidence in the residual errors. The main assumption in the algorithm is that the variability of the ionosphere at scales smaller than 200 km is limited or easy to model. The validity of this assumption—although difficult to evaluate in practice due to limited data sets with sufficient accuracy, coverage, and sampling rate–should be investigated further. The effects of double-differencing processing on other residual errors that have not been considered should also be investigated.

VI. System Performance

A simulation based on the PARIS-IoD scenario presented in Table III has been run, obtaining an instrument precision of 12.5 cm at the edge of the swath. Table VII shows the estimated final system altimetry performance of each reflection point when ionospheric delay residuals, tropospheric errors, and other sources of degradation (electromagnetic, skewness, and orbital errors) are taken into account. The ionospheric error includes the excess of pseudorange noise for a dual-frequency system and a regression over $N = 3$ points. The estimated total error is 17 cm at the edge of the swath, and 13 cm at nadir, for 100-km spatial resolution and three-day revisit time.

The perfomances have also been estimated in the case of an operational mission resulting in 7.5 cm at the edge of the swath and 5 cm at nadir, for 100-km spatial resolution and two-day revisit time.

VII. Conclusion

An ocean altimeter implementation of the original PARIS concept involving direct cross-correlation of the GNSS signals with their reflections off the Earth surface has been presented. It allows using the full power spectral density of all GNSS signals without the need to generate any code onboard, resulting in improved ranging precision and enhanced ionospheric delay correction. This is enabled by a particular antenna configuration based on a double phased array that is able to generate high-gain up- and downlooking beams. The beams are steered in real time owing to the time–position–velocity–attitude

TABLE VII
ESTIMATED SYSTEM PERFORMANCE BOTH FOR THE PARIS IoD SCENARIO OF TABLE III (LEFT COLUMN) AND FOR AN OPERATIONAL MISSION (RIGHT COLUMN). PERFORMANCE AT BOTH EDGE OF COVERAGE AND NADIR (IN BRACKETS) IS GIVEN

	IOD	**Operational**
Parameter	Height Accuracy on 100km, G=23dBi, h=800km	Height Accuracy on 100km, G=30dBi, h=1500km
Instrument Noise and Speckle	12.5 cm	4.2 cm
Ionosphere	9.7 cm (2 frequencies)	4.8 cm (3 frequencies)
Troposphere (Wet and Dry)	5 cm	2 cm
Electromagnetic Bias	2 cm	2 cm
Skewness Bias	2 cm	2 cm
Orbit	5 cm	2 cm
Total RMS Height Accuracy	**17 cm (13 cm at nadir)**	**7.5 cm (5 cm at nadir)**

information provided by the platform on-the-fly and the GNSS satellite ephemeris uplinked from ground to the payload computer. The antenna arrangement facilitates the use of a calibration switch and reference loads at the front end to perform accurate delay and amplitude calibration. Such an ocean altimeter is thought to provide accurate ranging and amplitude observations of GNSS reflected signals for a range of scientific applications besides mesoscale ocean altimetry. An in-orbit demonstration mission is proposed that would verify the performance to meet mesoscale ocean altimetry requirements. Such a demonstration mission would pave the way for a later operational one with full performance.

APPENDIX I
ANALYTICAL DERIVATION OF CROSS-CORRELATION STATISTICS

In this Appendix, the derivation of the generic relations adopted for the analysis of the interferometric processing power waveform is reported. The reflected power waveforms are derived by adopting a generic approach that describes the general statistics of the voltage cross-correlation function.

A. Transmitted GNSS Signal Representation

In order to formulate all the different GNSS transmitted signals in a simple but still general form, they are described by their nominal center frequency f_o and ambiguity function U, which will be defined later in (61). These parameters will suffice for the purpose of this paper. A generic transmitted signal is then expressed by its complex analytic representation

$$s(t) = \sqrt{2}\, u(t)\, e^{j2\pi f_o t} \tag{47}$$

where the function u has unity power and represents the complex baseband-modulated composite navigation signal of a particular satellite of a particular GNSS system. Therefore, its ACF is the composite ACF of all its modulating navigation codes.

Even if some codes are encrypted, this analysis is based on the properties of their ACF, which can be accurately measured without the need to know the originating codes.

B. Received Direct GNSS Signals

The received direct signal is represented as the sum of a delayed and attenuated version of the transmitted GNSS signal and of the receiver thermal noise of the direct channel

$$v_d(t) = s_d(t) + n_d(t) = A_d s(t - \tau_d) + n_d(t) \tag{48}$$

where the subscript d stands for "**d**irect." The term A_d is an amplitude factor (which, for instance, includes the GNSS signal transmitted power, the voltage antenna pattern of transmitting and receiving antennas, and the free-space loss), τ_d is the direct path delay, and n_d is the additive thermal noise.

As shown in Fig. 4, the received direct signal is successively downconverted according to the nominal frequency of the GNSS frequency band f_o and then further shifted by a frequency f_s to match the Doppler frequency corresponding to the specular point of the reflected signal. The Doppler shift is applied for a given instant time t_c, corresponding to the center of the interval over which the cross-correlation of the signals is performed, and is given by

$$f_s \equiv -\left.\frac{dr_s}{\lambda dt}\right|_{t=t_c} \tag{49}$$

where r_s is the excess distance of the reflected path through the specular point over the direct path.

The frequency-shifted received direct signal then becomes

$$\begin{aligned} v_d(t)&e^{j\varphi_o}e^{-j2\pi(f_o-f_s)t} \\ &= \left[A_d s(t-\tau_d) + n_d(t)\right] e^{j\varphi_o}e^{-j2\pi(f_o-f_s)t} \\ &= \sqrt{2}A_d\, u(t-\tau_d)\, e^{-j2\pi f_o \tau_d} e^{j\varphi_o} e^{j2\pi f_s t} \\ &\quad + n_d(t)e^{j\varphi_o}e^{-j2\pi(f_o-f_s)t} \end{aligned} \tag{50}$$

where φ_o is the phase of the LO. The direct signal is then time shifted by

$$T_s \equiv \left.\frac{r_s}{c}\right|_{t=t_c} \tag{51}$$

to align it with the reflected signal to which it will be cross-correlated, with c being the speed of light in vacuum. The direct signal at the input of the cross-correlator becomes

$$v_{d,c}(t) = \sqrt{2}A_d\, u(t-\tau_d-T_s)\, e^{-j2\pi f_o \tau_d} e^{j\varphi_o} e^{j2\pi f_s(t-T_s)} + n_d(t-T_s)e^{j\varphi_o}e^{-j2\pi(f_o-f_s)(t-T_s)} \tag{52}$$

where the signal and noise components at the input of the cross-correlator can be identified as

$$\begin{aligned} s_{d,c}(t) &= \sqrt{2}A_d\, u(t-\tau_d-T_s)\, e^{-j2\pi f_o \tau_d} e^{j\varphi_o} e^{j2\pi f_s(t-T_s)} \\ n_{d,c}(t) &= n_d(t-T_s)e^{j\varphi_o}e^{-j2\pi(f_o-f_s)(t-T_s)} \end{aligned} \tag{53}$$

with the subscript d, c standing for "**d**irect signal at **c**orrelator input." Fig. 5 shows the adopted reference geometry.

C. Received Ocean Scattered GNSS Signal

The received ocean scattered GNSS signal can be represented as a coherent summation of the reflected signal from elementary ocean scatters in the generic downlooking antenna beam, as expressed by the Kirchhoff approximation [10], [13], [32]

$$s_r(t) = \sqrt{2}\int_{\theta,\phi} W(\theta,\varphi,t)u\left(t-\tau_r(\theta,\varphi,t)\right)e^{j2\pi f_o(t-\tau_r(\theta,\varphi,t))}d\Omega \tag{54}$$

with

$$v_r(t) = s_r(t) + n_r(t)$$

where the subscript "r" stands for "**r**eflected," n_r is the receiver thermal noise, $d\Omega = \sin(\theta)d\theta d\varphi$, $W(\theta,\varphi,t)$ is a complex amplitude factor which includes all the radar equation parameters (i.e., the transmitting voltage antenna pattern of the GNSS satellite, path losses, the voltage antenna pattern of the PARIS receiving beam, and the complex reflectivity of the generic scatter over the ocean surface toward the PARIS satellite), and $\tau_r(\theta,\varphi,t)$ is the time delay of the generic reflecting path impinging the sea surface at position (θ,φ) and received at the PARIS satellite, as shown in Fig. 5. For notation simplicity, in the following, the spatial dependence θ,φ and time dependence t of the amplitude term $W(\theta,\varphi,t)$ and of the delay term $\tau_r(\theta,\varphi,t)$ will be denoted in the subscript as $W_{\theta,\varphi,t}$ and $\tau_{r,\theta,\varphi,t}$. The downconverted received reflected signal can be then represented by

$$\begin{aligned} v_{r,c}(t) &\equiv v_r(t)e^{j\varphi_o}e^{-j2\pi f_o t} \\ &= \sqrt{2}\int_{\theta,\phi} W_{\theta,\phi,t}u(t-\tau_{r,\theta,\phi,t})e^{j2\pi f_o(t-\tau_{r,\theta,\phi,t})} \\ &\quad\times e^{j\varphi_o}e^{-j2\pi f_o t}\, d\Omega + n_r(t)e^{j\varphi_o}e^{-j2\pi f_o t} \\ &= \sqrt{2}\int_{\theta,\phi} W_{\theta,\phi,t}u(t-\tau_{r,\theta,\phi,t})e^{-j2\pi f_o \tau_{r,\theta,\phi,t}}e^{j\varphi_o}\, d\Omega \\ &\quad + n_r(t)e^{j\varphi_o}e^{-j2\pi f_o t}. \end{aligned} \tag{55}$$

The useful signal and noise components at the input of the cross-correlator are therefore

$$\begin{aligned} s_{r,c}(t) &= \sqrt{2}\int_{\theta,\phi} W_{\theta,\phi,t}u(t-\tau_{r,\theta,\phi,t})e^{-j2\pi f_o \tau_{r,\theta,\phi,t}}e^{j\varphi_o}\, d\Omega \\ n_{r,c}(t) &= n_r(t)e^{j\varphi_o}e^{-j2\pi f_o t} \end{aligned} \tag{56}$$

having assumed that the oscillator phase φ_o is the same in both up- and downlooking chains.

D. Direct Complex Cross-Correlation

Following the representation introduced earlier, the direct complex cross-correlation can be expressed as the sum of four terms

$$\begin{aligned} Z(t,\tau) &= \frac{1}{T_c}\int_{-T_c/2}^{+T_c/2} v_{r,c}(t+t')\, v^*_{d,c}(t+t'-\tau)\, dt' \\ &= \frac{1}{T_c}\int_{-T_c/2}^{+T_c/2} s_{r,c}(t+t')\, s^*_{d,c}(t+t'-\tau)\, dt' \\ &\quad+ \frac{1}{T_c}\int_{-T_c/2}^{+T_c/2} s_{r,c}(t+t')\, n^*_{d,c}(t+t'-\tau)\, dt' \\ &\quad+ \frac{1}{T_c}\int_{-T_c/2}^{+T_c/2} n_{r,c}(t+t')\, s^*_{d,c}(t+t'-\tau)\, dt' \\ &\quad+ \frac{1}{T_c}\int_{-T_c/2}^{+T_c/2} n_{r,c}(t+t')\, n^*_{d,c}(t+t'-\tau)\, dt' \\ &= Z_S(t,\tau) + Z_{N\,d}(t,\tau) + Z_{N\,r}(t,\tau) + Z_{N\,dr}(t,\tau) \end{aligned} \tag{57}$$

where T_c is the cross-correlation integration time, referred to as the receiver coherent integration time in the following. The four terms of the voltage cross-correlation function in (57) are derived hereinafter.

1) Signal Voltage Cross-Correlation $Z_S(t,\tau)$: The signal component of the voltage cross-correlation is represented by the first term in (57). Using (52) and (55) yields

$$\begin{aligned} &Z_S(t,\tau) \\ &= \frac{1}{T_c}\int_{-T_c/2}^{+T_c/2} s_{r,c}(t+t')\, s^*_{d,c}(t+t'-\tau)\, dt' \\ &= \frac{2A_d}{T_c}\int_{-T_c/2}^{+T_c/2}\int_{\theta,\phi} W_{\theta,\phi,t+t'}u(t+t'-\tau_{r,\theta,\phi,t+t'}) \\ &\qquad\times e^{-j2\pi f_o \tau_{r,\theta,\phi,t+t'}}\, d\Omega \\ &\qquad\cdot u^*(t+t'-\tau-\tau_{d,t+t'-\tau}-T_s) \\ &\qquad\times e^{+j2\pi f_o \tau_{d,t+t'-\tau}}e^{-j2\pi f_s(t+t'-\tau-T_s)}\, dt' \end{aligned}$$

$$
\begin{aligned}
&= \frac{2A_d}{T_c} \int_{\theta,\phi} \int_{-T_c/2}^{+T_c/2} W_{\theta,\phi,t+t'} u(t+t'-\tau_{r,\theta,\phi,t+t'}) \\
&\qquad \times u^*(t+t'-\tau-\tau_{d,t+t'-\tau}-T_s) \\
&\qquad \cdot e^{-j2\pi f_o \tau_{r,\theta,\phi,t+t'}} e^{+j2\pi f_o \tau_{d,t+t'-\tau}} \\
&\qquad \times e^{-j2\pi f_s (t+t'-\tau-T_s)}\, dt'\, d\Omega
\end{aligned} \tag{58}
$$

having inverted the order of the integrals and expressed the dependence on spatial coordinates and on time at the subscript. Now, the following assumptions are safely taken:

$$
\begin{aligned}
W_{\theta,\varphi,t+t'} &\approx W_{\theta,\varphi,t} \\
\tau_{r,\theta,\varphi,t+t'} &\approx \tau_{r,\theta,\varphi,t} - \frac{f_{Dr,\theta,\varphi,t}}{f_o} t' \\
\tau_{d,t+t'-\tau} &\approx \tau_{d,t-\tau} - \frac{f_{Dd,t-\tau}}{f_o} t'
\end{aligned} \tag{59}
$$

where $f_{Dd,t}$ is the Doppler frequency of the direct signal at time t and $f_{Dr,\theta,\varphi,t}$ is the Doppler frequency of the generic reflecting path impinging the sea surface at position (θ, φ) and received at the PARIS satellite at time t, as shown in Fig. 5. Adopting (59) for the exponential terms, the cross-correlation in (58) becomes

$$
\begin{aligned}
&Z_S(t,\tau) \\
&= \frac{2A_d}{T_c} \\
&\quad \times \int_{\theta,\phi} W_{\theta,\phi,t} \int_{-T_c/2}^{+T_c/2} u(t+t'-\tau_{r,\theta,\phi,t+t'}) \\
&\qquad \times u^*(t+t'-\tau-\tau_{d,t+t'-\tau}-T_s) \\
&\qquad \times e^{+j2\pi[f_{Dr,\theta,\phi,t}-f_{Dd,t-\tau}-f_s]t'}\, dt' \\
&\qquad \cdot e^{+j2\pi f_o \tau_{d,t-\tau}} e^{-j2\pi f_s (t-\tau-T_s)} \\
&\qquad \times e^{-j2\pi f_o \tau_{r,\theta,\phi,t}}\, d\Omega \\
&= 2A_d \int_{\theta,\phi} W_{\theta,\phi,t} U(\Delta\tau, \Delta f, t) e^{+j2\pi f_o [\tau_{d,t-\tau}-\tau_{r,\theta,\phi,t}]} \\
&\qquad \times e^{-j2\pi f_s (t-\tau-T_s)}\, d\Omega
\end{aligned} \tag{60}
$$

where $U(\Delta\tau, \Delta f, t)$ is the Woodward ambiguity function of the composite GNSS signal, defined by

$$
U(\Delta\tau, \Delta f, t) = \frac{1}{T_c} \int_{-T_c/2}^{+T_c/2} u(t+t') u^*(t+t'-\Delta\tau)\, e^{-j2\pi\, \Delta f\, t'}\, dt' \tag{61}
$$

with

$$
\begin{aligned}
\Delta\tau &= \tau + \tau_{d,t-\tau} + T_s - \tau_{r,\theta,\varphi,t} \\
\Delta f &= -f_{Dr,\theta,\varphi,t} + f_{Dd,t-\tau} + f_s.
\end{aligned} \tag{62}
$$

2) Reflected Signal and Uplooking Noise Voltage Cross-Correlation $Z_{Nd}(t,\tau)$: The voltage cross-correlation of the direct channel thermal noise with the ocean reflected signal is given by

$$
Z_{N\,d}(t,\tau) = \frac{1}{T_c} \int_{-T_c/2}^{+T_c/2} s_{r,c}(t+t')\, n^*_{d,c}(t+t'-\tau)\, dt' \tag{63}
$$

and using (52), (55), and (59) yields

$$
\begin{aligned}
&Z_{N\,d}(t,\tau) \\
&= \frac{1}{T_c} \int_{-T_c/2}^{+T_c/2} s_{r,c}(t+t')\, n^*_{d,c}(t+t'-\tau)\, dt' \\
&= \frac{\sqrt{2}}{T_c} \int_{-T_c/2}^{+T_c/2} \int_{\theta,\phi} W_{\theta,\phi,t+t'} u(t+t'-\tau_{r,\theta,\phi,t+t'}) \\
&\qquad \times e^{-j2\pi f_o \tau_{r,\theta,\phi,,t+t'}}\, d\Omega \\
&\qquad \cdot n^*_d(t+t'-\tau-T_s) \\
&\qquad \times e^{+j2\pi (f_o-f_s)(t+t'-\tau-T_s)}\, dt' \\
&= \frac{\sqrt{2}}{T_c} \int_{\theta,\phi} W_{\theta,\phi,t} \int_{-T_c/2}^{+T_c/2} u(t+t'-\tau_{r,\theta,\phi,t+t'}) \\
&\qquad \times n^*_d(t+t'-\tau-T_s) \\
&\qquad \times e^{+j2\pi[f_{Dr,\theta,\phi,t}+f_o-f_s]t'}\, dt' \\
&\qquad \cdot e^{+j2\pi(f_o-f_s)(t-\tau-T_s)} \\
&\qquad \times e^{-j2\pi f_o \tau_{r,\theta,\phi,t}}\, d\Omega.
\end{aligned} \tag{64}
$$

3) Direct Signal and Downlooking Noise Voltage Cross-Correlation $Z_{Nr}(t,\tau)$: Similarly, the voltage cross-correlation of the reflected channel thermal noise with the direct signal is given by

$$
Z_{N\,r}(t,\tau) = \frac{1}{T_c} \int_{-T_c/2}^{+T_c/2} n_{r,c}(t+t')\, s^*_{d,c}(t+t'-\tau)\, dt' \tag{65}
$$

$$
\begin{aligned}
Z_{N\,r}(t,\tau) &= \frac{1}{T_c} \int_{-T_c/2}^{+T_c/2} n_{r,c}(t+t')\, s^*_{d,c}(t+t'-\tau)\, dt' \\
&= \frac{\sqrt{2}A_d}{T_c} \int_{-T_c/2}^{+T_c/2} n_r(t+t') \\
&\qquad \times u^*(t+t'-\tau-\tau_{d,t+t'-\tau}-T_s) \\
&\qquad \times e^{-j2\pi f_o (t+t')} e^{+j2\pi f_o \tau_{d,t+t'-\tau}} \\
&\qquad \times e^{-j2\pi f_s (t+t'-\tau-T_s)}\, dt'.
\end{aligned} \tag{66}
$$

4) Uplooking Noise and Downlooking Noise Voltage Cross-Correlation $Z_{Ndr}(t,\tau)$: The voltage cross-correlation of the reflected channel thermal noise with the direct channel thermal noise is

$$Z_{N\,dr}(t,\tau)=\frac{1}{T_c}\int_{-T_c/2}^{+T_c/2} n_{r,c}(t+t')\,n^*_{d,c}(t+t'-\tau)\,dt' \tag{67}$$

$$\begin{aligned}Z_{N\,dr}(t,\tau)&=\frac{1}{T_c}\int_{-T_c/2}^{+T_c/2} n_{r,c}(t+t')\,n^*_{d,c}(t+t'-\tau)\,dt'\\&=\frac{1}{T_c}\int_{-T_c/2}^{+T_c/2} n_r(t+t')e^{-j2\pi f_o(t+t')}\\&\qquad\times n^*_d(t+t'-\tau-T_s)\\&\qquad\times e^{+j2\pi(f_o-f_s)(t+t'-\tau-T_s)}\,dt'.\end{aligned} \tag{68}$$

E. Complex Cross-Correlation Statistics

By considering that the signal and the uplooking and downlooking thermal noise components in (57) are uncorrelated to each other, the statistics at the correlator output can be represented as the sum of four terms

$$\begin{aligned}\langle Z(t_1,\tau_1)Z^*(t_2,\tau_2)\rangle&=\langle Z_S(t_1,\tau_1)Z_S^*(t_2,\tau_2)\rangle\\&+\langle Z_{N\,d}(t_1,\tau_1)Z^*_{N\,d}(t_2,\tau_2)\rangle\\&+\langle Z_{N\,r}(t_1,\tau_1)Z^*_{N\,r}(t_2,\tau_2)\rangle\\&+\langle Z_{N\,dr}(t_1,\tau_1)Z^*_{N\,dr}(t_2,\tau_2)\rangle\end{aligned} \tag{69}$$

where the cross-correlations are considered evaluated at different center times t_1, t_2 and at different delay lags τ_1, τ_2. In the following, these four terms are derived.

1) Signal-Times-Signal Statistics: This section derives a general expression of the statistics of the signal component. By denoting $t_1=t$, $t_2=t+\tilde{t}$, $\tau_1=\tau$, and $\tau_2=\tau+\tilde{\tau}$ and substituting them in (60), the general statistics of the signal component $\langle Z_S(t,\tau)Z_S^*(t+\tilde{t},\tau+\tilde{\tau})\rangle$ can be written as

$$\begin{aligned}&\left\langle Z_S(t,\tau)Z_S^*\left(t+\tilde{t},\tau+\tilde{\tau}\right)\right\rangle\\&=\Bigg\langle 2A_d\int_{\theta_i,\phi_i} W_{i,t}U_{i,t}e^{+j2\pi f_o\,(\tau_{d,t-\tau}-\tau_{r,i,t})}\\&\qquad\times e^{-j2\pi f_s(t-\tau-T_s)}\,d\Omega_i\\&\quad\cdot 2A_d\int_{\theta_j,\phi_j} W^*_{j,t+\tilde{t}}U^*_{j,t+\tilde{t}}\\&\qquad\times e^{-j2\pi f_o(\tau_{d,t+\tilde{t}-\tau-\tilde{\tau}}-\tau_{r,j,t+\tilde{t}})}\\&\qquad\times e^{+j2\pi f_s(t+\tilde{t}-\tau-\tilde{\tau}-T_s)}\,d\Omega_j\Bigg\rangle\end{aligned}$$

$$\begin{aligned}&=4A_d^2\int_{\theta_i,\phi_i}\int_{\theta_j,\phi_j}\left\langle W_{i,t}W^*_{j,t+\tilde{t}}U_{i,t}U^*_{j,t+\tilde{t}}e^{+j2\pi f_o\,[\tau_{r,j,t+\tilde{t}}-\tau_{r,i,t}]}\right\rangle\\&\qquad\times e^{+j2\pi f_o\,[\tau_{d,t-\tau}-\tau_{d,t+\tilde{t}-\tau-\tilde{\tau}}]}e^{-j2\pi f_s(t-\tau-T_s)}\\&\qquad\times e^{+j2\pi f_s(t+\tilde{t}-\tau-\tilde{\tau}-T_s)}\,d\Omega_i\,d\Omega_j\end{aligned} \tag{70}$$

where the statistical average has been applied inside the spatial integrals. The dependence on spatial coordinates θ_i, φ_i and θ_j, φ_j is expressed by subscripts i and j, respectively. It is worth mentioning that the statistical expectations are with respect to the six random variables related to the random nature of the sea surface, namely, $W_{i,t}$, $W_{j,t+\tilde{t}}$, $\tau_{r,i,t}$, $\tau_{r,j,t+\tilde{t}}$, $f_{Dr,j,t}$, and $f_{Dr,j,t+\tilde{t}}$.

In the following, for simplicity, the random behavior of the Doppler frequency is neglected, and the Doppler frequency over the sea surface is described by means of its average value (i.e., the Doppler frequency corresponding to the mean sea surface level). This assumption is well justified because the statistical dispersion of the excess Doppler frequency due to the random elevation of a sea scatter is very small by comparison with its average Doppler frequency.

Under this assumption, the statistical average of (70) can be written in the form of a conditional expectation with respect to the delays $\tau_{r,i,t}$ and $\tau_{r,j,t+\tilde{t}}$ over the sea surface

$$\left\langle U_{i,t}U^*_{j,t+\tilde{t}}e^{+j2\pi f_o\,[\tau_{r,j,t+\tilde{t}}-\tau_{r,i,t}]}\left\langle W_{i,t}W^*_{j,t+\tilde{t}}\middle|\,\tau_{r,j,t+\tilde{t}},\tau_{r,i,t}\right\rangle\right\rangle. \tag{71}$$

The complex amplitude factor $W_{i,t}W^*_{j,t+\tilde{t}}$ can be considered independent from the delays $\tau_{r,i}$ and $\tau_{r,j}$, since, due to the geometrical properties of a space-based observation, the locus of points with the same generic delay always intersects a representative mixture of sea surface conditions (e.g., crests, sides, and valleys) regardless of the value of the delay. Therefore, (71) can be rewritten as a product of averages [13]

$$\left\langle U_{i,t}U^*_{j,t+\tilde{t}}e^{+j2\pi f_o\,[\tau_{r,j,t+\tilde{t}}-\tau_{r,i,t}]}\right\rangle\left\langle W_{i,t}W^*_{j,t+\tilde{t}}\right\rangle. \tag{72}$$

The first average term in (72) can be further simplified by representing the delays as the sum of two components

$$\tau_{r,\theta,\varphi,t}=\overline{\tau_{r,\theta,\varphi,t}}+u_{r,\theta,\varphi,t}=\overline{\tau_{r,\theta,\varphi,t}}-\frac{2\cos(\alpha_{\mathrm{inc}})}{c}z_{\theta,\varphi,t} \tag{73}$$

where $\overline{\tau_{r,\theta,\varphi,t}}$ is the delay of the reflected path corresponding to the local mean sea level, u_r is the additional delay due to the random sea surface height $z_{\theta,\varphi,t}$ with respect to the local mean sea level, and α_{inc} is the bistatic incidence angle with respect to the local surface. By showing the dependence of the argument of U with respect to u_r (and omitting for simplicity its dependence on Δf and t), the first average of (72) becomes

$$\begin{aligned}&\Big\langle U_{i,t}(\overline{\Delta\tau_{i,t}}-u_{r,i,t})U^*_{j,t+\tilde{t}}(\overline{\Delta\tau_{j,t+\tilde{t}}}-u_{r,j,t+\tilde{t}})\\&\quad\cdot e^{+j2\pi f_o\,[u_{r,j,t+\tilde{t}}-u_{r,i,t}]}\Big\rangle\cdot e^{+j2\pi f_o\,[\overline{\tau_{r,j,t+\tilde{t}}}-\overline{\tau_{r,i,t}}]}\end{aligned} \tag{74}$$

and if $p(u_{r,i}, u_{r,j})$ is the joint probability density function of $u_{r,i,t}$ and $u_{r,j,t}$, the statistical average in (74) is given by

$$\int_{-\infty}^{+\infty}\int_{-\infty}^{+\infty} p\left(u_{r,i}, u_{r,j}\right) U_{i,t}\left(\overline{\Delta\tau_{i,t}} - u_{r,i,t}\right) \cdot U^*_{j,t+\tilde{t}}\left(\overline{\Delta\tau_{j,t+\tilde{t}}} - u_{r,j,t+\tilde{t}}\right) \cdot e^{+j2\pi f_o\left[u_{r,j,t+\tilde{t}} - u_{r,i,t}\right]}\, du_{r,i}\, du_{r,j}. \tag{75}$$

It is noted that, in the case that the random components u_r's of the delays are statistically independent, the probability density function will be factorized to $p(u_{r,i})p(u_{r,j})$; therefore, the average expressed in (75) will factor into a product of two expectations. This case is always satisfied when the delays refer to two points (θ_i, φ_i) and (θ_j, φ_j) over the sea surface sufficiently spaced apart. In this case, the single average component would be given by $\langle U(\overline{\Delta\tau} - u_r)e^{-j2\pi f_o u_r}\rangle$. Under the assumption that the standard deviation of the sea surface height is equal or larger than the radar wavelength, this expectation will be zero, since the phase at the exponential term is uniformly distributed. Therefore, the integral in (75) will be nonnegligible only for the case where the random delay components are statistically correlated.

Assuming that the sea surface height is spatially uncorrelated for any point of the surface $(\theta_i, \varphi_i) \neq (\theta_j, \varphi_j)$ and that the time $\tilde{t}$ is much smaller than the correlation time of the sea surface (i.e., $u_r(t) \approx u_r(t + \tilde{t})$), then, for the purpose of integration, we may write

$$p(u_{r,i}, u_{r,j}) \approx p(u_{r,i})\delta(u_{r,i} - u_{r,j})$$

and substitution into (75) yields

$$\int p(u_{r,i}) U_{i,t}\left(\overline{\Delta\tau_i} - u_{r,i}\right) U^*_{j,t+\tilde{t}}\left(\overline{\Delta\tau_j} - u_{r,i}\right) du_{r,i}. \tag{76}$$

Considering that the spatial integrals are nonnegligible only for $(\theta_i, \varphi_i) = (\theta_j, \varphi_j)$, the complex voltage cross-correlation in (70) becomes

$$\begin{aligned}\left\langle Z_S(t,\tau) Z_S^*(t+\tilde{t}, \tau+\tilde{\tau})\right\rangle &= 4A_d^2 \int_{\theta,\phi} \left\langle W_{\theta,\varphi,t} W^*_{\theta,\varphi,t}\right\rangle \left[p(u_r) \underset{u_r}{\otimes} \left|U_{\theta,\varphi,t}\left(\overline{\Delta\tau} - u_r\right)\right|^2\right] \\ &\quad \cdot e^{+j2\pi f_o\left[\overline{\tau_{r,\theta,\varphi,t+\tilde{t}}} - \overline{\tau_{r,\theta,\varphi,t}}\right]}\, d\theta\, d\varphi \\ &\quad \cdot e^{+j2\pi f_o\left[\tau_{d,t-\tau} - \tau_{d,t+\tilde{t}-\tau-\tilde{\tau}}\right]} e^{+j2\pi f_s(\tilde{t}-\tilde{\tau})}\end{aligned} \tag{77}$$

where it has been assumed that the Woodward ambiguity function is slowly varying with time, i.e., $U_{i,t} \approx U_{i,t+\tilde{t}}$. Expressing the delay as a function of the Doppler frequency as

$$\begin{aligned}\overline{\tau_{r,\theta,\varphi,t+\tilde{t}}} &= \overline{\tau_{r,\theta,\varphi,t}} - \frac{f_{Dr,\theta,\varphi,t}}{f_o}\tilde{t} \\ \tau_{d,t+\tilde{t}-\tau-\tilde{\tau}} &= \tau_{d,t-\tau} - \frac{f_{Dd,t-\tau}}{f_o}(\tilde{t} - \tilde{\tau})\end{aligned} \tag{78}$$

(77) becomes

$$\begin{aligned}\left\langle Z_S(t,\tau) Z_S^*(t+\tilde{t}, \tau+\tilde{\tau})\right\rangle &= 4A_d^2 \int_{\theta,\phi} \left\langle W_{\theta,\varphi,t} W^*_{\theta,\varphi,t}\right\rangle \left[p(u_r) \underset{u_r}{\otimes} \left|U_{\theta,\varphi,t}\left(\overline{\Delta\tau} - u_r\right)\right|^2\right] \\ &\quad \cdot e^{+j2\pi\left[f_{Dd,t-\tau} - f_{Dr,\theta,\varphi,t} + f_s\right]\tilde{t}} e^{-j2\pi f_{Dd,t-\tau}\tilde{\tau}} \\ &\quad \cdot e^{-j2\pi f_s\tilde{\tau}}\, d\Omega.\end{aligned} \tag{79}$$

The aforementioned general expression can be particularized in order to analyze the statistical behavior of the cross-correlation function. For instance, if $\tilde{t} = 0$, the expression provides the lag-to-lag delay correlation. If, instead, $\tilde{\tau} = 0$, then (79) provides the so-called pulse-to-pulse voltage correlation. For both $\tilde{t} = 0$ and $\tilde{\tau} = 0$, the reflected average power waveform is instead derived

$$\begin{aligned}\left\langle \left|Z_S(t,\tau)\right|^2\right\rangle &= 4A_d^2 \int_{\theta,\phi} \left\langle \left|W_{\theta,\varphi,t}\right|^2\right\rangle \left[p(u_r) \underset{u_r}{\otimes} \left|U_{\theta,\varphi,t}\left(\overline{\Delta\tau} - u_r\right)\right|^2\right] d\Omega \\ &= 2P_D\left[2P_{R,\theta,\varphi} \underset{\theta,\varphi}{\otimes} \left[p(u_r) \underset{u_r}{\otimes} \left|U_{\theta,\varphi,t}\left(\overline{\Delta\tau} - u_r\right)\right|^2\right]\right]\end{aligned} \tag{80}$$

where P_D is the power of the received direct signal and $P_{R,\theta,\varphi} = \langle|W_{\theta,\varphi,t}|^2\rangle$ is the average reflected signal power received from a generic sea surface scatterer at position (θ, φ). Equivalent expressions can be found in [10], [21], and [28].

2) Uplooking Noise-Times-Signal Statistics: The statistics of the cross-correlation between the direct channel noise and the scattered signal are presented in the following. The statistical average can be written from (64) as

$$\begin{aligned}\left\langle Z_{Nd}(t,\tau) Z^*_{Nd}\left(t+\tilde{t}, \tau+\tilde{\tau}\right)\right\rangle &= \Bigg\langle \frac{2}{T_c^2} \int_{\theta_i,\phi_i} W_{i,t} \int_{-T_c/2}^{+T_c/2} u(t + t' - \tau_{r,i,t+t'}) \\ &\qquad \times n_d^*(t + t' - \tau - T_s) \\ &\qquad \times e^{+j2\pi\left[f_{Dr,i,t} + f_o - f_s\right]t'}\, dt' \\ &\qquad \times e^{+j2\pi(f_o - f_s)(t-\tau-T_s)} \\ &\qquad \times e^{-j2\pi f_o\tau_{r,i,t}}\, d\Omega_i \\ &\quad \cdot \int_{\theta_j,\phi_j} W^*_{j,t+\tilde{t}} \int_{-T_c/2}^{+T_c/2} u^*(t + \tilde{t} + t'' - \tau_{r,j,t+\tilde{t}+t''}) \\ &\qquad \times n_d(t + \tilde{t} + t'' - \tau - \tilde{\tau} - T_s) \\ &\qquad \times e^{-j2\pi\left[f_{Dr,j,t+\tilde{t}} + f_o - f_s\right]t''}\, dt'' \\ &\qquad \times e^{-j2\pi(f_o - f_s)(t+\tilde{t}-\tau-\tilde{\tau}-T_s)} \\ &\qquad \times e^{+j2\pi f_o\tau_{r,j,t+\tilde{t}}}\, d\Omega_j \Bigg\rangle.\end{aligned} \tag{81}$$

By inverting the order of the spatial integrals with the time integrals, (81) becomes

$$\begin{aligned}&\left\langle Z_{Nd}(t,\tau)Z^*_{Nd}(t+\tilde{t},\tau+\tilde{\tau})\right\rangle\\&=\frac{2}{T_c^2}\Bigg\langle\int\limits_{\theta_i,\phi_i}\int\limits_{\theta_j,\phi_j}W_{i,t}W^*_{j,t+\tilde{t}}\\&\quad\cdot\int\limits_{-T_c/2}^{+T_c/2}\int\limits_{-T_c/2}^{+T_c/2}u(t+t'-\tau_{r,i,t+t'})\\&\quad\times u^*(t+\tilde{t}+t''-\tau_{r,j,t+\tilde{t}+t''})\\&\quad\cdot n^*_d(t+t'-\tau-T_s)\\&\quad\times n_d(t+\tilde{t}+t''-\tau-\tilde{\tau}-T_s)\\&\quad\cdot e^{+j2\pi[f_{Dr,i,t}+f_o-f_s]t'}\\&\quad\times e^{-j2\pi[f_{Dr,j,t+\tilde{t}}+f_o-f_s]t''}\,dt'\,dt''\\&\quad\cdot e^{j2\pi f_o(\tau_{r,j,t+\tilde{t}}-\tau_{r,i,t})}\\&\quad\times e^{-j2\pi(f_o-f_s)(\tilde{t}-\tilde{\tau})}\,d\Omega_i\,d\Omega_j\Bigg\rangle.\end{aligned}\tag{82}$$

As presented before for the signal cross-correlation statistics, the statistical average can be written in the form of conditional expectation with respect to the delays $\tau_{r,i,t}$ and $\tau_{r,j,t+\tilde{t}}$ over the sea surface. It consequently follows that the average can be written as a product of expectations, with W_i, W_j, and n_d being independent with respect to these delays

$$\begin{aligned}&\langle Z_{Nd}(t_1,\tau_1)Z^*_{Nd}(t_2,\tau_2)\rangle\\&=2\int\limits_{\theta_i,\phi_i}\int\limits_{\theta_j,\phi_j}\left\langle W_{i,t}W^*_{j,t+\tilde{t}}\right\rangle\\&\quad\cdot\Bigg\langle\frac{1}{T_c^2}\int\limits_{-T_c/2}^{+T_c/2}\int\limits_{-T_c/2}^{+T_c/2}u(t+t'-\tau_{r,i,t+t'})\\&\quad\times u^*(t+\tilde{t}+t''-\tau_{r,j,t+\tilde{t}+t''})\\&\quad\cdot\langle n^*_d(t+t'-\tau-T_s)\\&\quad\times n_d(t+\tilde{t}+t''-\tau-\tilde{\tau}-T_s)\rangle\\&\quad\cdot e^{+j2\pi[f_{Dr,i,t}+f_o-f_s]t'}\\&\quad\times e^{-j2\pi[f_{Dr,j,t+\tilde{t}}+f_o-f_s]t''}\,dt'\,dt''\\&\quad\cdot e^{j2\pi f_o\left(\tau_{r,j,t+\tilde{t}}-\tau_{r,i,t}\right)}\\&\quad\times e^{-j2\pi(f_o-f_s)(\tilde{t}-\tilde{\tau})}\Bigg\rangle\,d\Omega_i\,d\Omega_j.\end{aligned}\tag{83}$$

The band-limited noise ACF can be expressed as

$$\begin{aligned}&\left\langle n^*_d(t+t'-\tau-T_s)n_d(t+\tilde{t}+t''-\tau-\tilde{\tau}-T_s)\right\rangle\\&\qquad=2kT_{Nd}\frac{\sin\left(2\pi B(t'-t''+\tilde{\tau}-\tilde{t})\right)}{\pi(t'-t''+\tilde{\tau}-\tilde{t})}.\end{aligned}\tag{84}$$

Then, substituting it into (83) and considering that $BT_c \gg 1$, the noise ACF can be simplified to a Dirac delta function for the purpose of the integration, yielding [37]

$$\begin{aligned}&\left\langle Z_{Nd}(t,\tau)Z^*_{Nd}(t+\tilde{t},\tau+\tilde{\tau})\right\rangle\\&=2\int\limits_{\theta_i,\phi_i}\int\limits_{\theta_j,\phi_j}\left\langle W_{i,t}W^*_{j,t+\tilde{t}}\right\rangle\\&\quad\cdot\Bigg\langle\frac{2kT_{Nd}}{T_c^2}\int\limits_{-T_c/2}^{+T_c/2}u(t+t'-\tau_{r,i,t+t'})\\&\quad\times u^*(t+t'+\tilde{\tau}-\tau_{r,j,t+t'+\tilde{\tau}})\\&\quad\cdot e^{+j2\pi[f_{Dr,i,t}+f_o-f_s]t'}\\&\quad\times e^{-j2\pi[f_{Dr,j,t}+f_o-f_s]t'}\,dt'\\&\quad\cdot e^{-j2\pi[f_{Dr,j,t}]\tilde{\tau}}e^{j2\pi f_o(u_{r,j,t}-u_{r,i,t})}\Bigg\rangle\\&\quad\cdot e^{j2\pi f_o(\overline{\tau_{r,j,t}}-\overline{\tau_{r,i,t}})}\,d\Omega_i\,d\Omega_j\cdot e^{-j2\pi(f_o-f_s)(\tilde{t}-\tilde{\tau})}\end{aligned}\tag{85}$$

having assumed

$$\begin{aligned}f_{Dr,\theta,\varphi,t+\tilde{t}}&\approx f_{Dr,\theta,\varphi,t}\\\tau_{r,\theta,\varphi,t+\tilde{t}}&\approx\overline{\tau_{r,\theta,\varphi,t}}+u_{r,\theta,\varphi,t}-\frac{f_{Dr,\theta,\varphi,t}}{f_0}\tilde{t}\end{aligned}\tag{86}$$

as for the signal cross-correlation case. Similarly, by considering the sea surface heights to be uncorrelated, (85) becomes

$$\begin{aligned}&\left\langle Z_{Nd}(t,\tau)Z^*_{Nd}(t+\tilde{t},\tau+\tilde{\tau})\right\rangle\\&=2\int\limits_{\theta,\phi}\left\langle W_{\theta,\phi,t}W^*_{\theta,\phi,t+\tilde{t}}\right\rangle\\&\quad\cdot\frac{2kT_{Nd}}{T_c^2}\Bigg\langle\frac{1}{T_c}\int\limits_{-T_c/2}^{+T_c/2}u(t+t'-\tau_{r,\theta,\phi,t+t'})\\&\quad\times u^*(t+t'+\tilde{\tau}+\tau_{r,\theta,\phi,t+t'+\tilde{\tau}})\,dt'\\&\quad\cdot e^{-j2\pi[f_{Dr,\theta,\phi,t}]\tilde{t}}\Bigg\rangle d\Omega\\&\quad\cdot e^{-j2\pi(f_o-f_s)(\tilde{t}-\tilde{\tau})}.\end{aligned}\tag{87}$$

Particularizing this general expression at $\tilde{\tau}=0$ and $\tilde{t}=0$, the average power yields

$$\begin{aligned}\left\langle Z_{Nd}(t,\tau)Z^*_{Nd}(t+\tilde{t},\tau+\tilde{\tau})\right\rangle&=\frac{2kT_{Nd}}{T_c}2\int\limits_{\theta,\phi}\left\langle|W_{\theta,\varphi,t}|^2\right\rangle d\Omega\\&=\frac{2kT_{Nd}}{T_c}2P_R\end{aligned}\tag{88}$$

where P_R is the total reflected power received in the main antenna beam at the input of the cross-correlator, i.e.,

$$P_R = \int_{\theta,\phi} \left\langle |W_{\theta,\varphi,t}|^2 \right\rangle d\Omega. \tag{89}$$

Equation (88) can be interpreted as the product of the reflected signal average power $2P_R$ at the input of the cross-correlator and the downlooking noise power at the output of the cross-correlator $(2kT_{Nd}/T_c)$.

3) Downlooking Noise-Times-Signal Statistics: The statistics of downlooking channel noise and direct signal cross-correlation are presented in the following. By considering (66) and following the same considerations done in the other cases, the cross-correlation power can be represented as

$$\left\langle Z_{Nr}(t,\tau) Z^*_{Nr}(t+\tilde{t}, \tau+\tilde{\tau}) \right\rangle = \frac{2kT_{Nr}}{T_c} 2P_D. \tag{90}$$

Equation (90) can be interpreted as the product of the direct signal average power $2P_D$ at the input of the cross-correlator and the uplooking noise power at the output of the cross-correlator, given by $(2kT_{Nr}/T_c)$.

4) Noise-Times-Noise Statistics: The statistics of downlooking channel noise and uplooking channel noise cross-correlation are presented in the following. By considering (68) and following the same considerations done in the other cases, the cross-correlation power can be represented as

$$\left\langle Z_{Ndr}(t,\tau) Z^*_{Ndr}(t+\tilde{t}, \tau+\tilde{\tau}) \right\rangle = \frac{2kT_{Nr}}{T_c} 2kT_{Nd}B. \tag{91}$$

Equation (91) can be interpreted as the product of the downlooking channel noise power at the output of the cross-correlator and the downlooking channel noise power at the input of the cross-correlator.

F. SNR of the Cross-Correlation

By considering (69), the SNR at the output of the cross-correlator is given by

$$SNR(t,\tau) = \frac{\left\langle |Z_S(\tau)|^2 \right\rangle}{\left\langle |Z_{Nd}(\tau)|^2 \right\rangle + \left\langle |Z_{Nr}(\tau)|^2 \right\rangle + \left\langle |Z_{Ndr}(\tau)|^2 \right\rangle}. \tag{92}$$

Substituting the derived equations (80), (88), (90), and (91), $SNR(t,\tau)$ becomes

$$SNR(t,\tau) = \frac{2P_D \bullet \left[2P_{R,\theta,\varphi} \underset{\theta,\varphi}{\otimes} \left[p(u_r) \underset{u_r}{\otimes} \left| U_{\theta,\varphi,t}(\overline{\Delta\tau} - u_r) \right|^2 \right] \right]}{2P_R \frac{2kT_{Nd}}{T_c} + 2P_D \frac{2kT_{Nr}}{T_c} + \frac{2kT_{Nd} 2kT_{Nr} B}{T_c}}. \tag{93}$$

Simple manipulations of (93) yield

$$SNR(t,\tau) = \frac{BT_c \left[2P_{R,\theta,\varphi} \underset{\theta,\varphi}{\otimes} \left[p(u_r) \underset{u_r}{\otimes} U^2_{\theta,\varphi,t}(\overline{\Delta\tau} - u_r) \right] \right]}{2kT_{Nr}B \left[1 + \frac{2P_R}{2kT_{Nr}B} \frac{2kT_{Nd}B}{2P_D} + \frac{2kT_{Nd}B}{2P_D} \right]}$$

$$= \frac{SNR_{cr}}{\left[1 + \frac{1+SNR_R}{SNR_D} \right]} \tag{94}$$

where SNR_{cr} is the SNR at the output of the cross-correlator that would have been obtained in the case of adoption of an onboard clean replica, given by

$$SNR_{cr}(t,\tau) = \frac{T_c \left[P_{R,\theta,\varphi} \underset{\theta,\varphi}{\otimes} \left[p(u_r) \underset{u_r}{\otimes} \left| U_{\theta,\varphi,t}\left(\overline{\Delta\tau} - u_r\right) \right|^2 \right] \right]}{kT_{Nr}} \tag{95}$$

and, on the other hand, SNR_R and SNR_D are, respectively, the SNR of the reflected signal and the SNR of the direct signal both at the input of the cross-correlator, given by

$$SNR_R = \frac{P_R}{kT_{Nr}B}$$
$$SNR_D = \frac{P_D}{kT_{Nd}B}. \tag{96}$$

As expected, it can be noticed from (94) that the SNR at the output of the cross-correlator is lower in the case of interferometric processing than the one obtainable with the use of a known clean replica onboard (i.e., SNR_{cr}). The degradation factor is given by the denominator in (94) and depends on the SNR of the direct and reflected signals at the input of the cross-correlator. The SNR degradation is negligible if the relation $SNR_D \gg 1 + SNR_R$ is satisfied by proper design of the front end.

Appendix II
Error Propagation in Three-Frequency Observations to Correct for Ionospheric Delay

The single-difference (reflected delay minus direct delay) equation is

$$\rho = -2h \cos i + \frac{I'}{f^2} \tag{97}$$

or

$$\frac{\rho}{2\cos i} = -h + \frac{I'}{2\cos i \; f^2} \tag{98}$$

which will be expressed by

$$y = -h + \frac{x}{f^2}. \tag{99}$$

The matrix system for the three frequencies is then

$$\begin{bmatrix} y_1 \\ y_2 \\ y_3 \end{bmatrix} = \begin{bmatrix} -1 & f_1^{-2} \\ -1 & f_2^{-2} \\ -1 & f_5^{-2} \end{bmatrix} \begin{bmatrix} h \\ x \end{bmatrix} \tag{100}$$

or

$$y = Mz \tag{101}$$

whose solution is given by

$$z = [M^{\mathrm{T}} M]^{-1} M^{\mathrm{T}} y. \tag{102}$$

The computation of the pseudoinverse matrix follows:

$$[M^{\mathrm{T}}M]^{-1}M^{\mathrm{T}} = \frac{1}{3Q-S^2}\begin{bmatrix} Q & S \\ S & 3 \end{bmatrix}\begin{bmatrix} -1 & -1 & -1 \\ f_1^{-2} & f_2^{-2} & f_5^{-2} \end{bmatrix} \tag{103}$$

with

$$S = f_1^{-2} + f_2^{-2} + f_5^{-2} \tag{104}$$
$$Q = f_1^{-4} + f_2^{-4} + f_5^{-4}. \tag{105}$$

The height and ionospheric delay estimations become

$$\begin{aligned} h &= \frac{-Q+Sf_1^{-2}}{3Q-S^2}\frac{\rho_1}{2\cos i} + \frac{-Q+Sf_2^{-2}}{3Q-S^2}\frac{\rho_2}{2\cos i} \\ &\quad + \frac{-Q+Sf_5^{-2}}{3Q-S^2}\frac{\rho_5}{2\cos i} \end{aligned} \tag{106}$$

$$\begin{aligned} x &= \frac{I'}{2\cos i} \\ &= \frac{-S+3f_1^{-2}}{3Q-S^2}\frac{\rho_1}{2\cos i} + \frac{-S+3f_2^{-2}}{3Q-S^2}\frac{\rho_2}{2\cos i} \\ &\quad + \frac{-S+3f_5^{-2}}{3Q-S^2}\frac{\rho_5}{2\cos i}. \end{aligned} \tag{107}$$

Assuming the same noise in all measured slant pseudoranges, the amplification factor for the height is

$$\frac{\sigma_h^2}{\sigma_y^2} = \frac{Q}{3Q-S^2} \tag{108}$$

and for the ionospheric delay

$$\frac{\sigma_x^2}{\sigma_y^2} = \frac{3}{3Q-S^2} \tag{109}$$

which leads to an ionospheric delay error at any particular frequency f of

$$f^{-4}\frac{\sigma_x^2}{\sigma_y^2} = \frac{3f^{-4}}{3Q-S^2}. \tag{110}$$

The S and Q coefficients take the following values:

$$\begin{aligned} f_1 &= 1575.42 \text{ MHz} \\ f_2 &= 1227.60 \text{ MHz} \\ f_5 &= 1176.45 \text{ MHz} \end{aligned} \tag{111}$$
$$S = f_1^{-2} + f_2^{-2} + f_5^{-2} = 1.789 \times 10^{-6} \text{ MHz}^{-2} \tag{112}$$
$$Q = f_1^{-4} + f_2^{-4} + f_5^{-4} = 1.1247 \times 10^{-12} \text{ MHz}^{-4}. \tag{113}$$

Therefore, the retrievals are

$$h = -2.33\frac{\rho_1}{2\cos i} + 0.36\frac{\rho_2}{2\cos i} + 0.97\frac{\rho_5}{2\cos i} \tag{114}$$
$$\frac{x}{f_1^2} = -1.35\frac{\rho_1}{2\cos i} + 0.47\frac{\rho_2}{2\cos i} + 0.88\frac{\rho_5}{2\cos i} \tag{115}$$
$$\frac{x}{f_2^2} = -2.22\frac{\rho_1}{2\cos i} + 0.77\frac{\rho_2}{2\cos i} + 1.45\frac{\rho_5}{2\cos i} \tag{116}$$
$$\frac{x}{f_5^2} = -2.42\frac{\rho_1}{2\cos i} + 0.84\frac{\rho_2}{2\cos i} + 1.58\frac{\rho_5}{2\cos i} \tag{117}$$

and the error propagation coefficients

$$\frac{\sigma_h}{\sigma_y} = 2.54 \tag{118}$$
$$\frac{1}{f_1^2}\sigma_x = 1.68\sigma_y \tag{119}$$
$$\frac{1}{f_2^2}\sigma_x = 2.76\sigma_y \tag{120}$$
$$\frac{1}{f_5^2}\sigma_x = 3\sigma_y. \tag{121}$$

Using the fact that the ionospheric delay is spatially correlated with itself but uncorrelated with the ocean topography, a regression over the ionospheric delay is taken. The idea is to preserve the precision of the height estimation per frequency as much as possible while getting rid of the ionospheric effect.

Starting with the triple-frequency system of equations (100), the ionospheric delay is first solved by (107). Then, a number of these (100-km resolution) ionospheric estimations around the current epoch are averaged through an adequate regression model regression: either $N = 3$ samples by linear fit or $N = 5$ samples by a fourth-order adjustment, for example. The new averaged ionospheric delay is then fed back into the single-difference equations of the current epoch

$$\frac{\rho}{2\cos i} = -h + \frac{\langle I' \rangle_N}{2\cos i\, f^2} \tag{122}$$

and the average height estimation across the three frequencies is taken

$$h_{125} = -\frac{1}{3}\frac{\rho_1+\rho_2+\rho_5}{2\cos i} + \frac{1}{3}\left(f_1^{-2}+f_2^{-2}+f_5^{-2}\right)\frac{\langle I' \rangle_N}{2\cos i} \tag{123}$$

resulting in an improved height precision of

$$\sigma_{h_{125}} = \sqrt{\frac{1}{3} + \frac{1.68^2}{9N} + \frac{2.76^2}{9N} + \frac{3^2}{9N}}\sigma_y \tag{124}$$

with N being the number of ionospheric delay samples used in the model fitting, i.e.,

$$\sigma_{h_{125}} = 1.03\sigma_y, \qquad \text{for } N = 3 \text{ (linear regression)} \tag{125}$$
$$\sigma_{h_{125}} = 0.87\sigma_y, \qquad \text{for } N = 5 \text{ (4th order regression)}. \tag{126}$$

The overall height precision becomes the same as that of the observables, or even improves.

Appendix III
Error Propagation in Two-Frequency Observations to Correct for Ionospheric Delay

The same derivation as that in Appendix B is shown here for two-frequency systems. The matrix system for the two-frequency case is

$$\begin{bmatrix} y_1 \\ y_2 \end{bmatrix} = \begin{bmatrix} -1 & f_1^{-2} \\ -1 & f_5^{-2} \end{bmatrix}\begin{bmatrix} h \\ x \end{bmatrix} \tag{127}$$
$$\begin{bmatrix} h \\ x \end{bmatrix} = \frac{1}{-f_5^{-2}+f_1^{-2}}\begin{bmatrix} f_5^{-2} & -f_1^{-2} \\ 1 & -1 \end{bmatrix}\begin{bmatrix} y_1 \\ y_2 \end{bmatrix}. \tag{128}$$

Assuming the same noise in the measured slant pseudoranges, the amplification factors are

$$\frac{\sigma_h^2}{\sigma_y^2} = \frac{Q'}{S'^2} \tag{129}$$

$$\frac{\sigma_x^2}{\sigma_y^2} = \frac{2}{S'^2} \tag{130}$$

with

$$S' = f_1^{-2} - f_5^{-2} = -3.19616 \times 10^{-7}\ \mathrm{MHz}^{-2} \tag{131}$$

$$Q' = f_1^{-4} + f_5^{-4} = 6.84379 \times 10^{-13}\ \mathrm{MHz}^{-4}. \tag{132}$$

The retrieved parameters are

$$h = -2.26\frac{\rho_1}{2\cos i} + 1.26\frac{\rho_5}{2\cos i} \tag{133}$$

$$\frac{x}{f_1^2} = -1.26\frac{\rho_1}{2\cos i} + 1.26\frac{\rho_5}{2\cos i} \tag{134}$$

$$\frac{x}{f_5^2} = -2.26\frac{\rho_1}{2\cos i} + 2.26\frac{\rho_5}{2\cos i}. \tag{135}$$

The error propagation equations are

$$\frac{\sigma_h}{\sigma_y} = 2.59 \tag{136}$$

$$\frac{1}{f_1^2}\sigma_x = 1.78\sigma_y \tag{137}$$

$$\frac{1}{f_5^2}\sigma_x = 3.2\sigma_y. \tag{138}$$

If N samples of ionospheric delay estimations (with 100-km spatial resolution) provided by (134) or (135) are averaged through an adequate regression and fed back into the single-difference equations of the present epoch, the average height estimation across the two frequencies yields

$$h_{15} = -\frac{1}{2}\frac{\rho_1 + \rho_5}{2\cos i} + \frac{1}{2}\left(f_1^{-2} + f_5^{-2}\right)\frac{\langle I' \rangle_N}{2\cos i}. \tag{139}$$

The precision of this height estimation is given by

$$\sigma_h = \sqrt{\frac{1}{2} + \frac{1.78^2}{4N} + \frac{3.2^2}{4N}}\sigma_y \tag{140}$$

that is

$$\sigma_{h_{15}} = 1.27\sigma_y, \qquad \text{for } N = 3 \text{ (linear regression)} \tag{141}$$

$$\sigma_{h_{125}} = 1.08\sigma_y, \qquad \text{for } N = 5 \text{ (4th order regression)}. \tag{142}$$

Acknowledgment

The authors would like to thank G. Toso (ESTEC, TEC-EEA) for the contribution on the antenna subsystem and S. Prowald (ESTEC, TEC-MCS) regarding the antenna structure and deployment mechanisms.

References

[1] V. Rosmorduc, J. Benveniste, O. Lauret, M. Milagro, and N. Picot, Radar Altimetry Tutorial, 2006.

[2] P. Y. Le Traon and G. Dibarboure, "An illustration of the unique contribution of the TOPEX/Poseidon—Jason-1 tandem mission to mesoscale variability studies," *Mar. Geod.*, vol. 27, pp. 3–13, 2004.

[3] M. Martín-Neira, C. Mavrocordatos, and E. Colzi, "Study of a constellation of bistatic radar altimeters for mesoscale ocean applications," *IEEE Trans. Geosci. Remote Sens.*, vol. 36, no. 6, pp. 1898–1904, Nov. 1998.

[4] European Space Agency Earth Explorers Portal. [Online]. Available: http://www.esa.int/esaLP/ESAMNM1VMOC_LPcryosat_0.html

[5] W. J. Emery, D. G. Baldwin, and D. K. Matthews, "Sampling the mesoscale ocean surface currents with various satellite altimeter configurations," *IEEE Trans. Geosci. Remote Sens.*, vol. 42, no. 4, pp. 795–803, Apr. 2004.

[6] C. Buck, "An extension to the wide swath ocean altimeter concept," in *Proc. IGARSS*, Seoul, Korea, 2005, pp. 5436–5439.

[7] M. Martín-Neira, "A passive reflectometry and interferometry system (PARIS): Application to ocean altimetry," *ESA J.*, vol. 17, pp. 331–335, 1993.

[8] S. Gleason, S. Hodgart, Y. Sun, C. Gommenginger, S. Mackin, M. Adjrad, and M. Unwin, "Detection and processing of bistatically reflected GPS signals from low earth orbit for the purpose of ocean remote sensing," *IEEE Trans. Geosci. Remote Sens.*, vol. 43, no. 6, pp. 1229–1241, Jun. 2005.

[9] S. Gleason, "Reflecting on GPS—Sensing land and ice from low earth orbit," *GPS World, Innovation Column*, vol. 18, no. 10, pp. 44–49, Oct. 2007.

[10] V. Zavorotny and A. G. Voronovich, "Scattering of GPS signals from the ocean with wind remote sensing application," *IEEE Trans. Geosci. Remote Sens.*, vol. 38, no. 2, pp. 951–964, Mar. 2000.

[11] T. Elfouhaily, B. Charpon, and K. Katsaros, "A unified directional spectrum for long and short wind-driven waves," *J. Geophys. Res.*, vol. 102, no. C7, pp. 15 781–15 796, 1997.

[12] GALILEO Open Service, Signal in Space Interface Control Document, OS SISI CD, Draft 1, Feb. 2008. [Online]. Available: http://www.gsa.europa.eu/go/galileo/os-sis-icd

[13] T. Berger, "Satellite altimetry using ocean backscatter," *IEEE Trans. Antennas Propag.*, vol. AP-20, no. 3, pp. 295–309, May 1972.

[14] F. Soulat, "Sea surface remote sensing with GNSS and sunlight reflections," Doctoral thesis, Universitat Politecnica de Catalunia, Starlab, Barcelona, Spain, Oct. 2003.

[15] E. Rodriguez and J. M. Martin, "Correlation properties of ocean altimeter returns," *IEEE Trans. Geosci. Remote Sens.*, vol. 32, no. 3, pp. 553–561, May 1994.

[16] P. Y. Le Traon, G. Dibarboure, G. Ruffini, and E. Cardellach, "Mesoscale ocean altimetry requirements and impact of GPS-R measurements for ocean mesoscale circulation mapping," Technical Note Extract from the PARIS-BETA ESTEC/ESA Study ESTEC, Dec. 2002. [Online]. Available: http://arxiv.org/abs/physics/0212068

[17] P. Y. Le Traon, G. Dibarboure, G. Ruffini, O. Germain, A. Thompson, and C. Mathew, "GNSS-R measurements for ocean mesoscale circulation mapping, an update," Technical Note Extract from the PARIS-GAMMA ESTEC/ESA Study, Sep. 2003.

[18] C. Zuffada and V. Zavorotny, "Coherence Time and Statistical properties of the GPS signal scattered off the ocean surface and their impact on the accuracy of remote sensing of sea surface topography and winds," in *Proc. Int. Geosci. Remote Sens. Symp.*, Jul. 9–13, 2001, vol. 7, pp. 3332–3334.

[19] S. T. Lowe, J. L. LaBrecque, C. Zuffada, L. J. Romans, L. Young, and G. A. Hajj, "First spaceborne observation of an earth-reflected GPS signal," *Radio Sci.*, vol. 37, no. 1, p. 1007, Feb. 2002a.

[20] O. Germain and G. Ruffini, "A revisit to the GNSS-R code range precision," in *Proc. GNSS-R Workshop*, Jun. 14–15, 2006. [Online]. Available: http://arxiv.org/abs/physics/0606180v1

[21] G. A. Hajj and C. Zuffada, "Theoretical description of a bistatic system for ocean altimetry using the GPS signal," *Radio Sci.*, vol. 38, no. 5, p. 1089, Oct. 2003.

[22] J. Betz, B. Barker, J. C. J. Correia, J. Gillis, S. Lazar, L. Rehborn, and J. Straton, Overview of the GPS M code signal, MITRE Corporation, McLean, VA, Tech. Rep. [Online]. Available: http://www.mitre.org/work/tech_papers/tech_papers_00/betz_overview/betz_overview.pdf

[23] A. E. Services, Navstar GPS space segment/user segment L1C interfaces, GPS Joint Program Office, El Segundo, CA, Tech. Rep., draft IS-GPS-800.

[24] D. Chelton, E. Walsh, and J. MacHartur, "Pulse compression and sea level tracking in satellite altimetry," *J. Atmos. Ocean. Technol.*, vol. 6, pp. 406–438, Jun. 1998.

[25] P. C. Marth, J. R. Jensen, C. C. Kilgus, J. A. Perschy, J. L. MacArthur, D. W. Hancock, G. S. Hayne, C. L. Purdy, L. C. Rossi, and C. J. Koblinsky, "Prelaunch performance of the NASA altimeter for the TOPEX/POSEIDON project," *IEEE Trans. Geosci. Remote Sens.*, vol. 31, no. 2, pp. 315–332, Mar. 1993.

[26] R. E. Fischer, "Standard deviation of scatterometer measurements from space," *IEEE Trans. Geosci. Electron.*, vol. GE-10, no. 2, pp. 106–113, Apr. 1972.
[27] S. J. Frasier and A. J. Camps, "Dual-beam interferometry for ocean surface current vector mapping," *IEEE Trans. Geosci. Remote Sens.*, vol. 39, no. 2, pp. 401–414, Feb. 2001.
[28] H. You, J. L. Garrison, G. Heckler, and V. U. Zavorotny, "Stochastic voltage model and experimental measurement of ocean-scattered GPS signal statistics," *IEEE Trans. Geosci. Remote Sens.*, vol. 42, no. 10, pp. 2160–2169, Oct. 2004.
[29] H. You, L. Garrison, G. Heckler, and D. Smajlovic, "The autocorrelation of waveform generated from ocean-scatters GPS signals," *IEEE Geosci. Remote Sens. Lett.*, vol. 3, no. 1, pp. 78–82, Jan. 2006.
[30] H. You, J. L. Garrison, G. Heckler, and V. U. Zavorotny, "Stochastic model and experimental measurement of ocean-scattered GPS signal statistics," in *Proc. IGARSS*, 2003, pp. 4492–4494.
[31] B. Wilmhoff, F. Lalezari, V. Zavorotny, and E. Walsh, "GPS ocean altimetry from aircraft using the P(Y) code signal," in *Proc. IEEE IGARSS*, Jul. 23–28, 2007, pp. 5093–5096.
[32] G. Picardi, R. Seu, S. G. Sorge, and M. M. Neira, "Bistatic model of ocean scattering antennas and propagation," *IEEE Trans. Antennas Propag.*, vol. 46, no. 10, pp. 1531–1541, Oct. 1998.
[33] F. T. Ulaby, R. K. Moore, and A. K. Fung, *Microwave Remote Sensing, Active and Passive*. Reading, MA: Addison-Wesley, 1982.
[34] L. Fu and A. Cazenave, *Satellite Altimetry and Earth Sciences*. New York: Academic, 2001.
[35] D. A. Imel, "Evaluation of the TOPEX/POSEIDON dual-frequency ionosphere correction," *J. Geophys. Res.*, vol. 99, no. C12, pp. 24 895–24 906, Dec. 1994.
[36] J. W. Goodman, *Statistical Optics*. New York: Wiley-Interscience, 1985.
[37] J. Minkoff, *Signals, Noise and Active Sensors*. New York: Wiley-Interscience, 1992.
[38] A. Rius, E. Cardellach, and M. Martín-Neira, "Altimetric analysis of sea surface GPS reflected signals," *IEEE Trans. Geosci. Remote Sens.*, vol. 48, no. 4, pp. 2119–2127, Apr. 2010.
[39] M. Brown, F. Torres, I. Corbella, and A. Colliander, "SMOS calibration," *IEEE Trans. Geosci. Remote Sens.*, vol. 46, no. 3, pp. 646–658, Mar. 2008.
[40] F. Torres, I. Corbella, A. Camps, N. Duffo, M. Vall-Llossera, S. Beraza, C. Gutierrez, and M. Martin-Neira, "Denormalization of visibilities for in-orbit calibration of interferometric radiometers," *IEEE Trans. Geosci. Remote Sens.*, vol. 44, pt. 1, no. 10, pp. 2679–2686, Oct. 2006.
[41] F. Bassiri and G. A. Hajj, "Higher-order ionospheric effects on the global positioning system observables and means of modeling them," *Manuscripta Geodaetica*, vol. 18, no. 6, pp. 280–289, 1993.
[42] M. Mainul Hoque and N. Jakowski, "Higher order ionospheric effects in precise GNSS positioning," *J. Geod.*, vol. 81, no. 4, pp. 259–268, 2007.
[43] E. D. Kaplan and C. J. Hegarty, *Understanding GPS Principles and Applications*. Norwood, MA: Artech House, 2006.
[44] M. Kocandrlova and S. Olivik, "Three geometrical approaches to the bi-static altimetry on the ellipsoid," in *Proc. GNSS-R Workshop*, Sep. 24–25, 2008, Presentation at GNSS-R 2008, 24-25 Sep, ESTEC.
[45] Final Report Use of bi-static microwave measurements for earth observation, Rome, Italy, 2007, Final Report.

Manuel Martín-Neira (SM'07) received the M.S. and Ph.D. degrees in telecommunication engineering from the School of Telecommunication Engineering, Polytechnic University of Catalonia, Barcelona, Spain, in 1986 and 1996, respectively.

In 1988, he was awarded a fellowship to work on radiometry at the European Space Research and Technology Centre (ESTEC), European Space Agency (ESA), Noordwijk, The Netherlands. From 1989 to 1992, he was with Grupo Mecánica de Vuelo (GMV), a Spanish firm, where he was responsible for several projects for the ESA related to GPS spacecraft navigation with applications to precise landing and attitude determination. Since 1992, he has been in charge of the radiometer activities within the Payload, Equipment and Technology Section of ESA. During this period, he has also developed new concepts for constellations of small satellites for Earth observation. In particular, he is the holder of a patent on the Passive Reflectometry and Interferometry System concept for the use of Global Navigation Satellite Systems signals reflected from the ocean. Currently, he is the Instrument Principal Engineer of ESA's Soil Moisture and Ocean Salinity Earth Explorer Opportunity Mission.

Dr. Martín-Neira has been a member of the Academie des Technologies of France since 2009. He received the Confirmed Inventor Award from the director of ESA in 2002

Salvatore D'Addio (M'07) received the Laurea degree (*summa cum laude*) in telecommunications engineering from the University of Naples, Naples, Italy, in 2005 and the M.S. degree in satellites and orbiting platforms from the Sapienza University of Rome, Rome, Italy, in 2006.

He is currently a Member of the Technical Staff of the Radio Frequency Payload Systems Division, European Space Research and Technology Centre, European Space Agency, Noordwijk, The Netherlands. From 2004 to 2006, he was involved in the radio-frequency testing of 3G UMTS mobile terminals and in optoelectronic sensor design and development. His current research interests include modeling, analysis, and design of advanced telecommunication satellite payloads and Earth-observation radio-frequency active and passive instruments.

Christopher Buck was born in Cambridge, U.K., in 1961. He received the B.S. degree in electronic and electrical engineering from the University of Surrey, Guildford, U.K., in 1984 and the M.Sc. degree in geographical information systems from Vrije Universiteit, Amsterdam, The Netherlands, in 2002.

Since 1994, he has been with the Radio Frequency Payload Systems Division, European Space Research and Technology Centre, European Space Agency, Noordwijk, The Netherlands, working in the area of microwave remote sensing. Originally on the ERS-2 AMI-SAR and later ENVISAT ASAR, he has also been responsible for various microwave remote sensing activities in the areas of SAR calibration and interferometry. Most recently, his research activities have been mainly directed toward wide-swath altimetry.

Mr. Buck is currently the Chairman of the Microwave Instrument Subgroup of the Committee on Earth Observation Satellites' Working Group on Calibration and Validation and also the Cochair of the Global Navigation Satellite Systems Working Group of the Instrumentation and Future Technologies Technical Committee of the IEEE Geoscience and Remote Sensing Society.

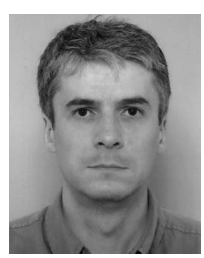

Nicolas Floury (M'07) received the Diplôme d'Ingénieur from the Ecole Nationale Supérieure des Télécommunications, Paris, France, in 1993 and the Ph.D. degree from the Université Paris 7 Denis Diderot, Paris, in 1999.

Since then, he has been with the European Space Research and Technology Centre, European Space Agency, Noordwijk, The Netherlands, where he is currently heading the Wave Interaction and Propagation Section. This section contributes to research and development in the fields of electromagnetic (optical to microwave) propagation through and interaction with natural media (atmosphere, land, and sea surface) and supports, on these aspects, the agency's programs in the domains of satellite telecommunication, navigation, and Earth observation. He has published on the applications of synthetic aperture radars and of microwave radiometers to remote sensing. His technical interests include signal processing and electromagnetic modeling applied to microwave interaction with natural media.

Roberto Prieto-Cerdeira (M'09) was born in Ourense, Spain, in 1978. He received the B.S. degree in telecommunications engineering from the University of Vigo, Vigo, Spain, in 2002. After one year working in the IT industry, he followed postgraduate studies on space science and radioastronomy at Chalmers University of Technology, Gothenburg, Sweden.

Since 2004, he has been with the Wave Interaction and Propagation Section, European Space Research and Technology Centre, European Space Agency, Noordwijk, The Netherlands, where he is currently responsible of radiowave propagation activities for ionospheric and local environment effects for satellite communications and for Galileo and EGNOS satellite navigation projects.